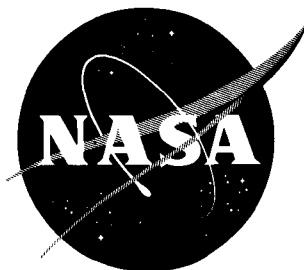


554198 P58

NASA TN D-1799

57p.



N 63 16427

Code-1

TECHNICAL NOTE

D-1799

SOME EFFECTS OF SIMULATED BENDING AND FOURTH-STAGE SIZE
ON LOCAL PRESSURES AND NORMAL-FORCE DISTRIBUTIONS
OF A MODEL OF A SCOUT CONFIGURATION
AT A MACH NUMBER OF 3.10

By Byron M. Jaquet

Langley Research Center
Langley Station, Hampton, Va.

NATIONAL AERONAUTICS AND SPACE ADMINISTRATION
WASHINGTON

May 1963

NATIONAL AERONAUTICS AND SPACE ADMINISTRATION

TECHNICAL NOTE D-1799

SOME EFFECTS OF SIMULATED BENDING AND FOURTH-STAGE SIZE

ON LOCAL PRESSURES AND NORMAL-FORCE DISTRIBUTIONS

OF A MODEL OF A SCOUT CONFIGURATION

AT A MACH NUMBER OF 3.10

By Byron M. Jaquet

SUMMARY

16427

A wind-tunnel investigation was made at a Mach number of 3.10 to determine the effects of simulated body bending and size of the fourth stage on the normal-force distributions of a 0.02655-scale model of the Scout research vehicle. Pressures were measured, with the straight-center-line model, on a 13° base flare and on the horizontal-tail panels with and without the base flare. Normal-force, axial-force, and pitching-moment coefficients were determined for a straight-center-line model of the Scout with and without the base flare and fourth-stage modifications. Most of the tests were conducted for a Reynolds number per foot of 23.4×10^6 .

It was found that body bending primarily affected the normal-force distribution at an angle of attack of 0° although there was some effect of body bending on the variation of the normal-force distribution with angle of attack. (There were many regions along the body in which loadings were not measured.) An increase in cone angle and size of the fourth stage increased the local normal-force coefficient as would be expected. The pressures on the horizontal tail were affected to a large extent by the addition of the base flare. The flare under certain conditions doubled the pressure coefficient and appeared to cause an outward and forward shift in the tail center of pressure. Pressures on the flare were generally highest near the horizontal-tail panels. Total force and pitching-moment coefficients were found to be affected more by the addition of the 13° base flare than by fourth-stage modifications of the straight model. Since the data were obtained on the bent-center-line model with a mode-shape deflection magnified by a factor of 20, the significance of the changes in normal-force distribution due to body bending cannot be assessed without a dynamic analysis of the vehicle along the launch trajectory.

INTRODUCTION

Missiles of high fineness ratio are subject to longitudinal bending during the atmospheric portion of their flight and the effect of the resulting periodic loads on the guidance and control requirements is of major concern. Significant effects of body camber on normal-force distributions can be inferred from the data of reference 1 for airplane-type bodies. The investigation of reference 2 indicated that body bending caused significant changes in the normal-force distributions of a two-stage launch-vehicle configuration. Reference 2 also indicated that the loadings on the bent body could not be accurately predicted and, therefore, that it is necessary to determine experimentally the effects of body bending on the normal-force distributions of a given vehicle.

The Scout launch vehicle was chosen for the present investigation of the effect of body bending on normal-force distributions since the first bending mode shape was readily available from dynamic analyses of the structural behavior. These data were obtained from an unpublished investigation similar to that of reference 3 by the authors of reference 3. Two scaled models of the Scout were constructed for the present investigation. One had a straight longitudinal center line and the other had a longitudinal center line that was bent to simulate the first bending mode shape at the condition of maximum dynamic pressure during the launch phase, which corresponds to a Mach number slightly higher than that of the present investigation. Local pressures were measured at a Mach number of 3.10 and a Reynolds number per foot of 23.4×10^6 . The effect of an increase in size of the fourth stage on the normal-force distributions was also determined. Some pressures were measured on the horizontal tail of the straight configuration with and without a 13° base flare (some pressures were also measured on the flare) in order to investigate the tail effectiveness in the presence of the flare. Also, normal and axial forces and pitching moments were measured on a straight model of the Scout with and without the base flare and fourth-stage modifications.

SYMBOLS

The coefficients are referred to the body system of axes shown in figure 1. The symbols used herein are defined as follows:

A	area of base of stage 1, sq in.
b	exposed span of horizontal tail, in.
c	local chord of horizontal tail, in.
D	diameter of base of stage 1, in.
l	model length, in.
M	Mach number
p	free-stream static pressure, lb/sq in.

p_l	local surface pressure, lb/sq in.
q	free-stream dynamic pressure, lb/sq in.
R	Reynolds number
r	radius of base of stage 1, in.
x	longitudinal distance from model nose; local distance from leading edge of horizontal tail, in.
y	lateral distance along horizontal tail, in.
α	angle of attack of straight reference line for both straight and bent models, deg
ϕ	radial angle indicating location of orifice, measured clockwise from vertical at top of model when viewed from nose toward base, deg
C_A	axial-force coefficient, $\frac{\text{Axial force}}{qA}$
$C_{A,b}$	base axial-force coefficient, $\frac{\text{Base axial force}}{qA}$
C_m	pitching-moment coefficient, $\frac{\text{Pitching moment}}{qAD}$ (see fig. 3 for location of moment reference)
C_N	normal-force coefficient, $\frac{\text{Normal force}}{qA}$
c_n	local normal-force coefficient, $\frac{\text{Local normal force}}{2qr}$
C_p	pressure coefficient, $\frac{p_l - p}{q}$
ΔC_p	incremental pressure coefficient between lower and upper surface of tail assuming that $C_{p,L}$ at $-\alpha$ is equivalent to $C_{p,U}$ at $+\alpha$ and vice versa for $-\alpha$

Subscripts:

U	upper surface
L	lower surface
α	partial derivative of principal symbol with respect to angle of attack

MODELS, EQUIPMENT, AND TESTS

The Scout is a four-stage launch vehicle utilizing solid propellants. Two basic models of the Scout were used in the local loading part of the investigation. (See fig. 2.) The first model had a straight longitudinal center line and the other had a longitudinal center line which was bent to simulate the first bending mode shape of the Scout at maximum dynamic pressure during launch (fig. 2(b)). The model deflections were magnified by a factor of 20 since the values scaled to the present model size were not large enough to produce a significant change in shape from the straight model. The mode shape was obtained from dynamic analyses made in the development program of the Scout. In order to facilitate model construction, the mode shape near the base of stage 1 and from the nose to the base of stage 4 was made linear. Dural nose gloves were fitted over the basic straight and bent models to determine the effects of changing the size of the fourth stage on the normal-force distributions. A 13° base flare was also fitted with orifices and was used on both models (fig. 2(a)). The details of construction of the models and the locations of the pressure orifices are shown in figure 2. Also shown in the figure are the simulated wiring tunnels that extended from the base of stage 4 to the base of stage 1.

A model with the same dimensions as the straight pressure model was constructed of dural and steel tubing (fig. 3) to be used with an electrical strain-gage balance to measure total forces. The tail fins were silver soldered to the steel tubing. It was noted after assembly that there existed a differential deflection of about $1\frac{1}{4}^\circ$ (the data have not been corrected for this) between the horizontal-tail panels, with the left panel down at the nose and with the right panel essentially at zero deflection. This model was also mounted rigidly to a sting and had orifices (closed for force tests) located on the upper surface of the horizontal tail in order to determine the influence of the base flare on the local tail pressures.

The pressures on the models were measured with pressurized Mercury manometer boards. All models were sting supported and the sting was hydraulically driven through a small angle-of-attack range. The tests were conducted in a blowdown jet, the test section of which had a height of about 12.5 inches and a width of 12 inches, at a Mach number of 3.10 and a stagnation temperature of about 100° F. Each configuration was tested over a small angle-of-attack range for the conditions indicated in the following table:

Configuration	13° base flare	Stagnation pressure, lb/sq in. gage	Test
Straight Scout	Off On	150 150	Local pressure
Bent Scout	Off On	149 149	
Straight Scout with nose glove	Off On	150 150	
Bent Scout with nose glove	Off On	149 150	
Straight Scout	Off Off	76 150	Tail pressure
Straight Scout	On On	76 150	
Straight Scout	Off On	150 149	Total force
Straight Scout with nose glove	Off On	150 149	

The pressure tests consisted of taking photographs of the manometer boards after a given angle of attack had been attained and after a period of about 25 seconds to reduce lag effects. Only the data taken after the delay period are presented herein. In order to obtain the angle of attack, shadowgraphs covering about 9 inches of the model from a point about $11\frac{1}{2}$ inches forward of the base were taken simultaneously with the manometer-board photographs.

For the force tests, normal force, axial force, and pitching moment were measured with an internal strain-gage balance over a small angle-of-attack range for the aforementioned test conditions. Base pressures were measured and the axial forces were adjusted to correspond to the free-stream static pressure. The angle of attack for these tests was determined from a sting position indicator and was corrected for deflection of the sting and balance under load.

The force test model was used to measure pressures at seven orifices located on the top surface of the horizontal-tail panels and was mounted rigidly to a sting. Tail pressures were measured for the test conditions over a small angle-of-attack range.

The Reynolds number per foot for most of the tests was about 23.4×10^6 . Some tail pressure tests were also made at a Reynolds number per foot of about 12.9×10^6 .

ACCURACY

Pressure Tests

The uncertainty in the angle of attack in the pressure tests was about $\pm 0.15^\circ$. The pressure coefficients are generally believed to be accurate to within ± 0.005 .

Force Tests

The uncertainty in the angle of attack in the force tests was about $\pm 0.10^\circ$. The measured coefficients are believed to be accurate within the following limits:

C_A	± 0.006
C_N	± 0.020
C_m	± 0.040

RESULTS AND DISCUSSION

Presentation of Results

The data are presented and discussed in three groups, as follows:

(1) Local pressure coefficients at $\phi = 0^\circ$ and $\alpha = 0^\circ$ for 4 model configurations (fig. 4); local pressure coefficients as functions of ϕ for 12 longitudinal stations at several angles of attack (figs. 5 to 8); local pressure coefficients as functions of ϕ for 4 stations on the 13° base flare and several angles of attack (figs. 9 to 12); tail pressure coefficients for the straight model as functions of angle of attack (figs. 13 and 14); tail pressure coefficients for the straight model as functions of y/b and x/c for several angles of attack (figs. 15 to 22); and $\Delta C_{p\alpha}$ as a function of y/b and x/c (fig. 23).

(2) Local normal-force coefficient c_n as a function of x/l at $\alpha = 0^\circ$ for the bent configurations (fig. 24) and the variation of $c_{n\alpha}$ with x/l for several straight and bent model configurations (fig. 25).

(3) Total coefficients as functions of α for several straight model configurations (fig. 26).

Local Pressure Coefficients

Body pressures.- The effect of body bending on the local pressure coefficients at $\phi = 0^\circ$ and $\alpha = 0^\circ$ is shown in figure 4 for the basic and enlarged fourth-stage configurations. These data indicate that body bending caused a decrease in the value of the pressure coefficient for stations forward of the midpoint and an increase for stations rearward of the midpoint. This is as would be expected since the stations forward of the midpoint on the bent body were at positive angles of attack and the rearward stations were at negative angles of attack with respect to the center line of the straight models which is the angle-of-attack reference line for all data presented. (See model drawing in fig. 2(b).) Cone theory values (ref. 4) of the pressure coefficients on the frustums at $\alpha = 0^\circ$ for the straight models are also included in figure 4. The cone theory of reference 4 overestimates the value of C_p on the nose of both straight models but gives a reasonably good estimate of the change in C_p due to an increase in size of the fourth stage. The effect of the small spherical nose of both models on the theoretical value of C_p was not considered. The antennas on the enlarged fourth-stage model caused a positive change in C_p at $0.135 < x/l < 0.155$ for both the straight and bent models.

The variation of C_p with ϕ for various longitudinal stations and angles of attack are presented, for the sake of completeness, in figures 5 to 8. These data are not discussed except to note that there were a number of leaks which could not be repaired. These are readily apparent. Also there were regions in which orifices were not located where the faired curves were extrapolated somewhat beyond the data points. It should also be noted that some orifices were located on the simulated wiring tunnels which extended from $\phi = 36^\circ$ to $\phi = 54^\circ$. The base flare had no measurable effect on the upstream pressure coefficients and thus only figures 5 to 8 were presented which were determined with the base flare off. The normal components of these faired curves (plots of C_p as a function of ϕ) were integrated to obtain loading coefficients discussed in a subsequent section.

Flare pressures.- Flare pressures were determined for two radial positions at each of four longitudinal stations on the flare. The data of figures 9 to 12 indicate that in regions of the flare near the fins there is generally an increase in pressure probably due to interference from the fins.

Tail pressures.- In order to indicate more clearly the effect of the base flare on the tail pressures, the basic tail-pressure data of figures 13 and 14 have been replotted in figures 15 to 22 as functions of the tail parameters y/b and x/c for selected angles of attack. For a given orifice location an increase in Reynolds number from 1.140×10^6 to 2.071×10^6 generally caused a small decrease in the value of C_p . The data of figures 15 to 22 indicate that the addition of the base flare causes an increase in the local pressures on the upper surface of the tail (pressures on the lower surface were not measured); this pressure increase would indicate an increase in lift effectiveness of the tail due to the presence of the flare. (A comparison of the data of figures 13 and 14 also shows a large change in the variation of C_p with α when the flare is added.) The effect of the flare is about the same for either test Reynolds number.

It is not possible to determine whether the increased effectiveness outboard of the flare is equal or not to the loss in effectiveness of the tail by the area covered by the flare.

With the assumption that $C_{p,L}$ at α is equivalent to $C_{p,U}$ at $-\alpha$, the derivative ΔC_{p_α} was determined which represents the slope of the incremental pressure coefficient plotted against angle of attack. The data of figure 23 indicate that the addition of the flare causes an increase in loading for outboard and forward locations of the tail and also tends to shift the center of pressure outboard and forward for regions investigated. These data should be used with caution since they were measured at only seven points on the tail. Also, the fin misalignment previously mentioned has apparently caused a difference in pressure coefficient between corresponding points on the left and right tail panels. (See data for $x/c = 0.65$ and $y/b = 0.40$.)

Local Normal-Force Distributions

The local normal-force coefficients presented in figures 24 and 25 were determined from the pressure coefficients presented in figures 5 to 8. As noted in the section entitled "Models, Equipment, and Tests," it was necessary to magnify the scaled bent model deflections by a factor of 20 in order to produce deflections significantly different from those of the straight model. Since sufficient longitudinal stations could not be fitted into the particular size of model used in the present investigation, it is not possible to determine an accurate total force coefficient by an integration of the normal-force-coefficient distributions of figures 24 and 25. For the straight models in figure 25, fitted curves were determined with the aid of the experimental total force and moment coefficients of reference 5 for similar shapes and with the local normal-force coefficients measured in the present investigation. The normal-force coefficients for stations in which local loads were not measured were selected so that the center-of-pressure locations and total normal-force coefficients for stages 3 and 4 ($0 < x/l < 0.28$) were identical to those measured in reference 5. The normal-force distributions on the small frustums for $0.22 < x/l < 0.28$ were proportioned according to slender body theory. When these fitted curves were integrated, the total coefficients and center-of-pressure locations were not in exact agreement with previously determined unpublished total normal-force-coefficient slopes and center-of-pressure locations. (Reference 6 presents results of an early investigation of a pointed-nose configuration; these results are similar to the unpublished values.) The present total normal-force-coefficient slopes were high by about 25 percent and the centers of pressure were forward by about three-fourths of 1 base diameter. It should be noted that the present test Reynolds number was about $\frac{1}{2}$ times that for the unpublished tests. Because of these differences the data of figures 24 and 25 should be used only to indicate changes in normal-force coefficient at the specific stations where data were measured.

The investigation of reference 1 for cambered relatively low fineness-ratio bodies (compared with the slender bodies investigated herein) indicated that the effects of body bending were primarily an increment in the total coefficients at

zero angle of attack with no appreciable effect on the slope of the total coefficients with angle of attack. The data indicate that, as would be expected for the bent slender bodies of the present investigation, there is a normal-force distribution at $\alpha = 0^\circ$ (fig. 24). (The normal-force distribution on the straight bodies is, of course, zero at $\alpha = 0^\circ$.) In addition, there are significant differences, except near the nose and the base, in the variation of the normal-force distribution with angle of attack between the bent body and the straight body (fig. 25).

The data for the bent model were obtained with the model shape magnified by a factor of 20 over that determined in a dynamic analysis of the vehicle. When reduced to account for this factor, the incremental loads would be small but no judgment relative to their significance can be made on this basis. Some insight into the significance of these loadings might be obtained from a dynamic analysis of the launch trajectory in which the loads would be properly weighted. The local angle of attack may be represented by three components: one due to the angle of attack of the vehicle as a whole, another due to body bending (camber), and a third arising from the translational velocity normal to the center line of the section. The measured incremental bent-body loadings of the present investigation might be used in a dynamic analysis to account for the second and third angle-of-attack components by weighting the local bent-body loadings by the sum of these two angles of attack. Distributions obtained from slender body theory ($\alpha = 0^\circ$) are included for comparison purposes in figure 24 for the basic fourth-stage configuration. When integrated, the slender-body-theory distributions give a value of $C_N = -0.033$ at $\alpha = 0^\circ$. Reference 1 indicates that slender body theory overpredicted the value of C_N at $\alpha = 0^\circ$ by about 25 percent. As previously mentioned, lack of a sufficient number of longitudinal stations precludes such a comparison for the present models.

A comparison of the data of figure 25 ($M = 3.10$) for the straight basic fourth-stage model with the data of reference 7 ($M = 1.20$) indicates that lower loadings generally occur at the present higher Mach number for regions where comparisons are possible.

Total Coefficients for Straight Model

The total force and pitching-moment data of figure 26 were affected more by the addition of the 13° base flare than by an increase in size of the fourth stage. An increase in size of the fourth stage had an appreciable effect on the value of C_A and C_m but had essentially no effect on C_N at a given angle of attack. The addition of the 13° base flare caused a large increase in C_A , a large rearward shift in the center-of-pressure location, a highly nonlinear variation of C_m with α , and a large increase in $C_{N\alpha}$. (The increment in C_m and C_N at $\alpha = 0^\circ$ is probably due to the fin misalignment.) The fourth-stage changes essentially redistributed the loading, whereas the flare increased as well as redistributed the loading.

The effects of the fourth-stage changes and the addition of the base flare on the aerodynamic parameters are summarized in the following table:

Fourth stage	13° base flare	C_A ($\alpha = 0^\circ$)	$C_{m\alpha}$ ($\alpha = 0^\circ$)	$C_{N\alpha}$ ($\alpha = 0^\circ$)	Center-of-pressure location from base, stage 1 base diameters
Basic	Off	0.280	0.169	0.091	8.1
Enlarged	Off	.390	.267	.091	9.2
Basic	On	.460	-.034	.131	6.0
Enlarged	On	.590	.054	.131	6.7

The values of C_A , $C_{N\alpha}$, and center-of-pressure location for the basic fourth-stage model without the base flare are in reasonably good agreement with the data of reference 6.

CONCLUDING REMARKS

A wind-tunnel investigation of the effect of simulated body bending and size of the fourth stage on the local normal-force distributions of a model of the Scout launch vehicle has indicated that body bending primarily affected the normal-force distribution at an angle of attack of 0° although some additional effect on the variation of the normal-force distribution with angle of attack was indicated. An increase in the size of the fourth stage of the model increased the normal-force coefficient over the nose portion as would be expected. It was also found that the addition of a 13° base flare affected the pressures on the horizontal tail. The flare under certain conditions doubled the pressure coefficient and appeared to cause an outboard and forward shift in the tail center of pressure. Pressures on the 13° base flare were generally largest near the horizontal-tail panels. Total force and pitching-moment coefficients were found to be affected more by the addition of the 13° base flare than by fourth-stage changes of the straight-center-line model.

Although the data on the bent-center-line model were obtained with a mode-shape deflection magnified by a factor of 20, the significance of the changes in normal-force distribution due to body bending cannot be assessed without a dynamic analysis of the vehicle along the launch trajectory.

Langley Research Center,
National Aeronautics and Space Administration,
Langley Station, Hampton, Va., March 12, 1963.

REFERENCES

1. Gapcynski, John P.: The Effect of Camber on the Aerodynamic Characteristics of a Body at a Mach Number of 2.01. NASA TM X-56, 1959.
2. Rainey, A. Gerald: Aeroelastic Research at High Speeds. NASA TM X-326, 1960.
3. Alley, Vernon L., Jr., and Gerringer, A. Harper: A Matrix Method for the Determination of the Natural Vibrations of Free-Free Unsymmetrical Beams With Application to Launch Vehicles. NASA TN D-1247, 1962.
4. Ames Research Staff: Equations, Tables, and Charts for Compressible Flow. NACA Rep. 1135, 1953. (Supersedes NACA TN 1428.)
5. Jaquet, Byron M.: Aerodynamic Characteristics at a Mach Number of 3.10 of Several Fourth-Stage Shapes of the Scout Research Vehicle. NASA TN D-916, 1961.
6. Jernell, Lloyd S., and Wong, Norman: Investigation of the Static Longitudinal Stability Characteristics of a 0.067-Scale Model of a Four-Stage Configuration of the Scout Research Vehicle at Mach Numbers of 2.29, 2.96, 3.96, and 4.65. NASA TN D-554, 1960.
7. Kelly, Thomas C.: Aerodynamic Loading Characteristics at Mach Numbers From 0.80 to 1.20 of a 1/10-Scale Three-Stage Scout Model. NASA TN D-945, 1961.

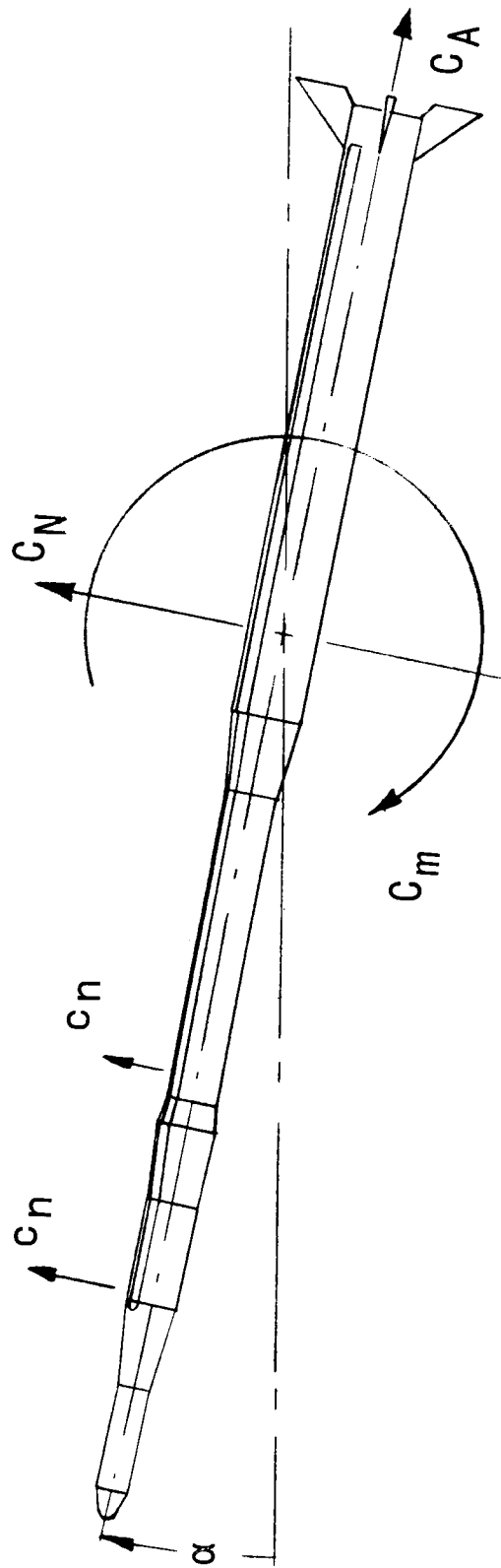
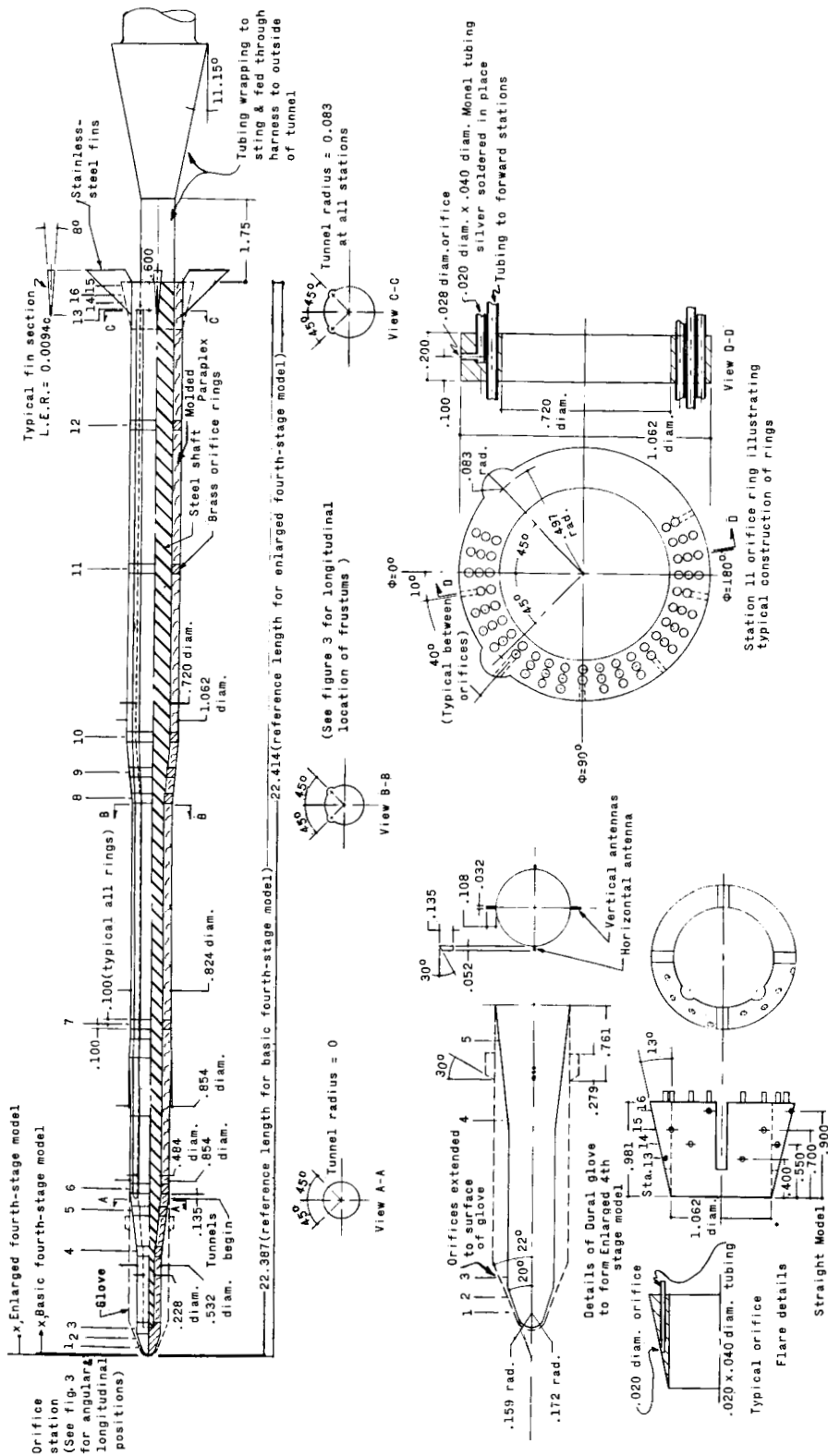
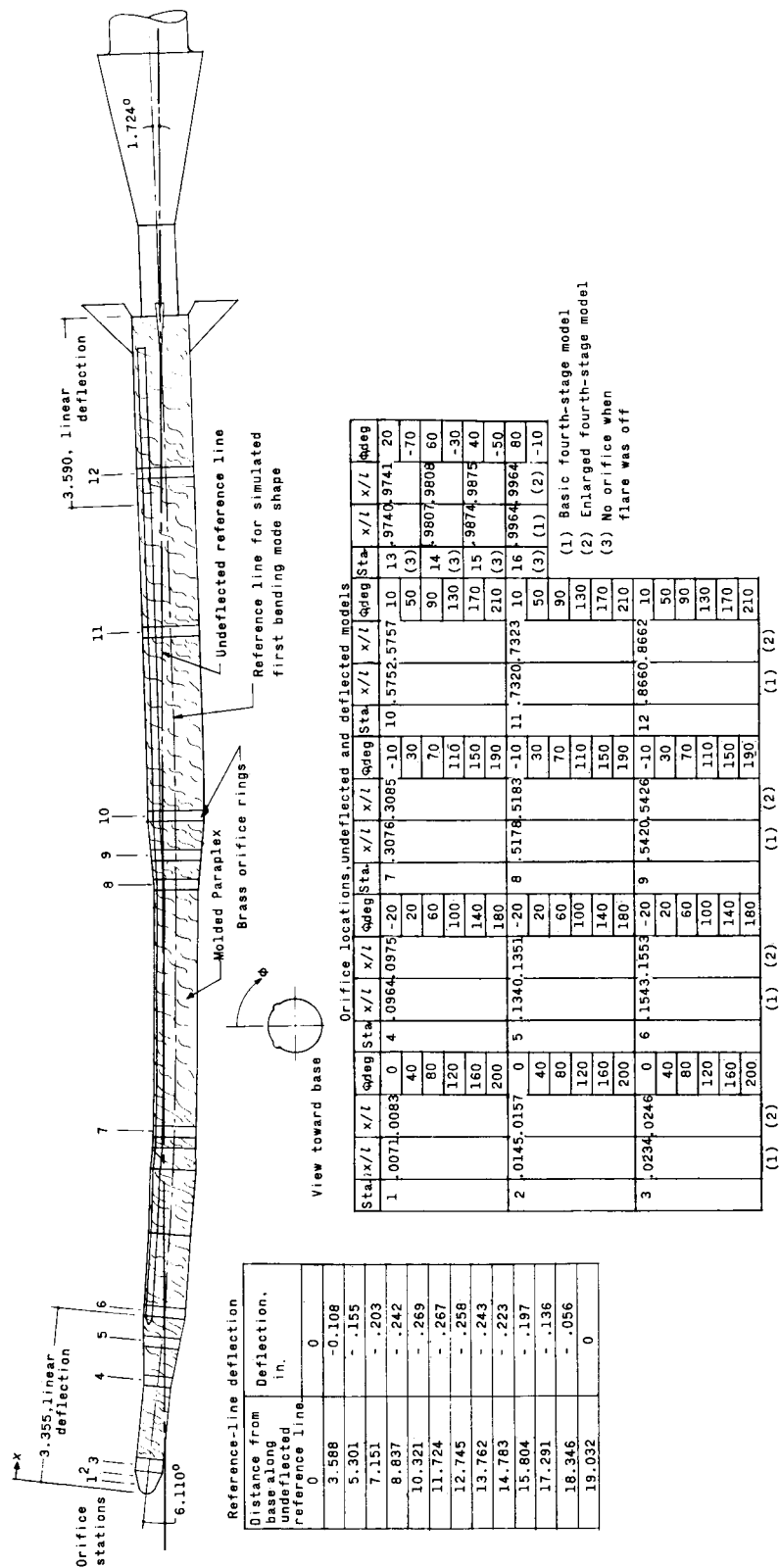


Figure 1.- System of axes illustrating positive coefficients and angle of attack.



(a) Straight model.

Figure 2.- General arrangement of a 0.02655-scale model of the Scout launch vehicle used for pressure measurements. Dimensions are in inches unless noted otherwise.



(b) General arrangement of model simulating first bending mode.

Figure 2.- Concluded.

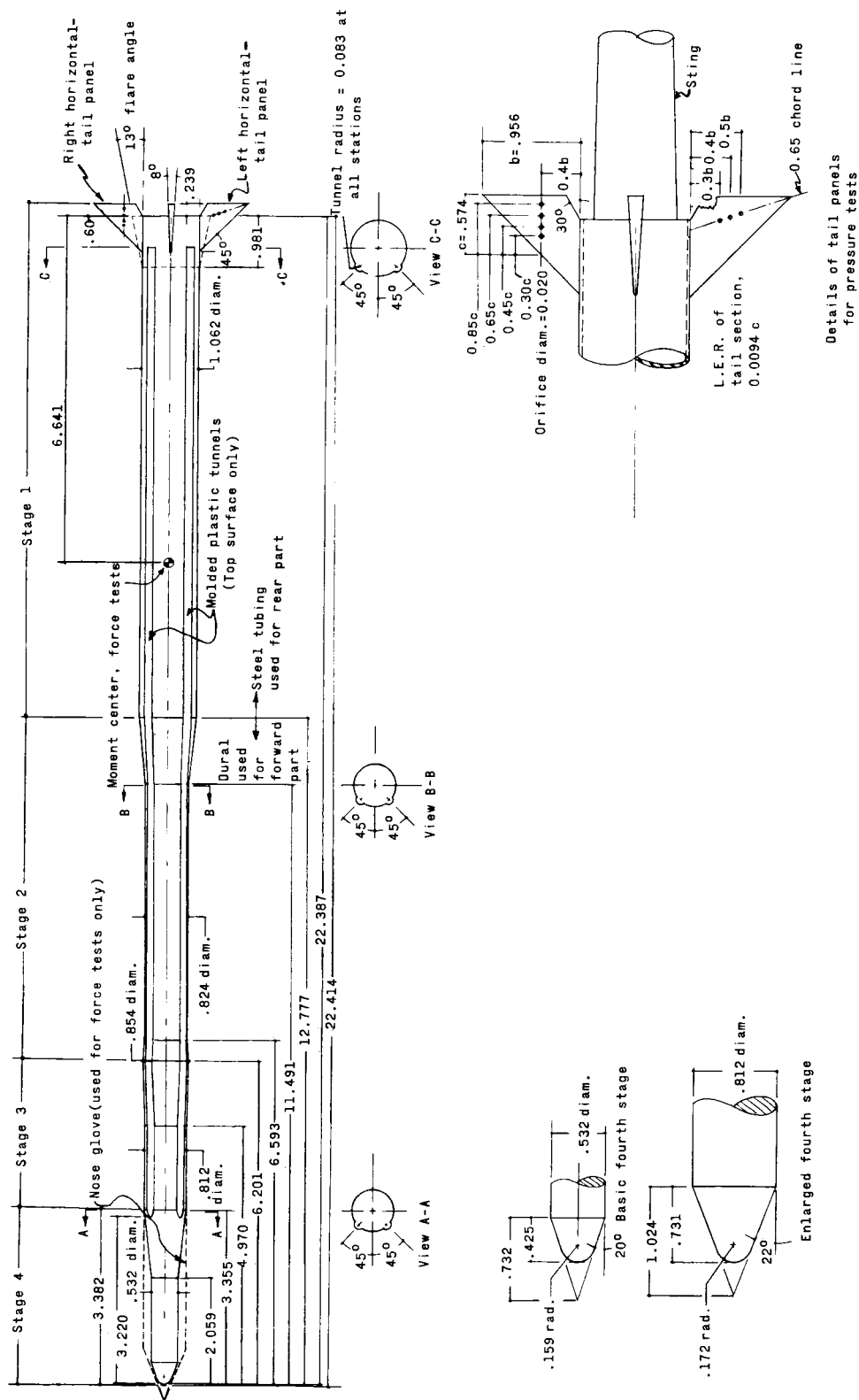


Figure 3.- General arrangement of 0.0265-scale complete models used for force and tail pressure tests. All dimensions are in inches unless otherwise noted.

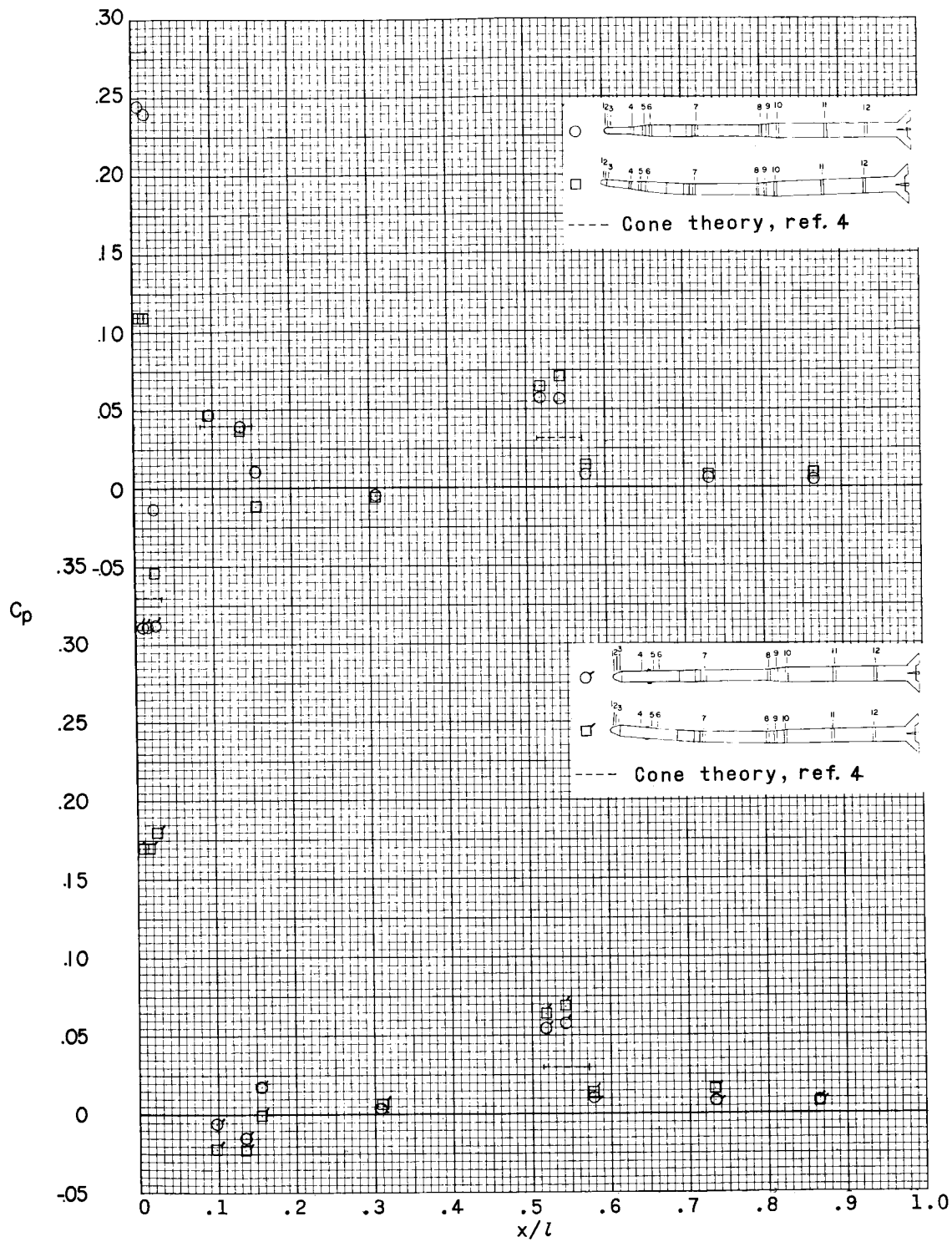
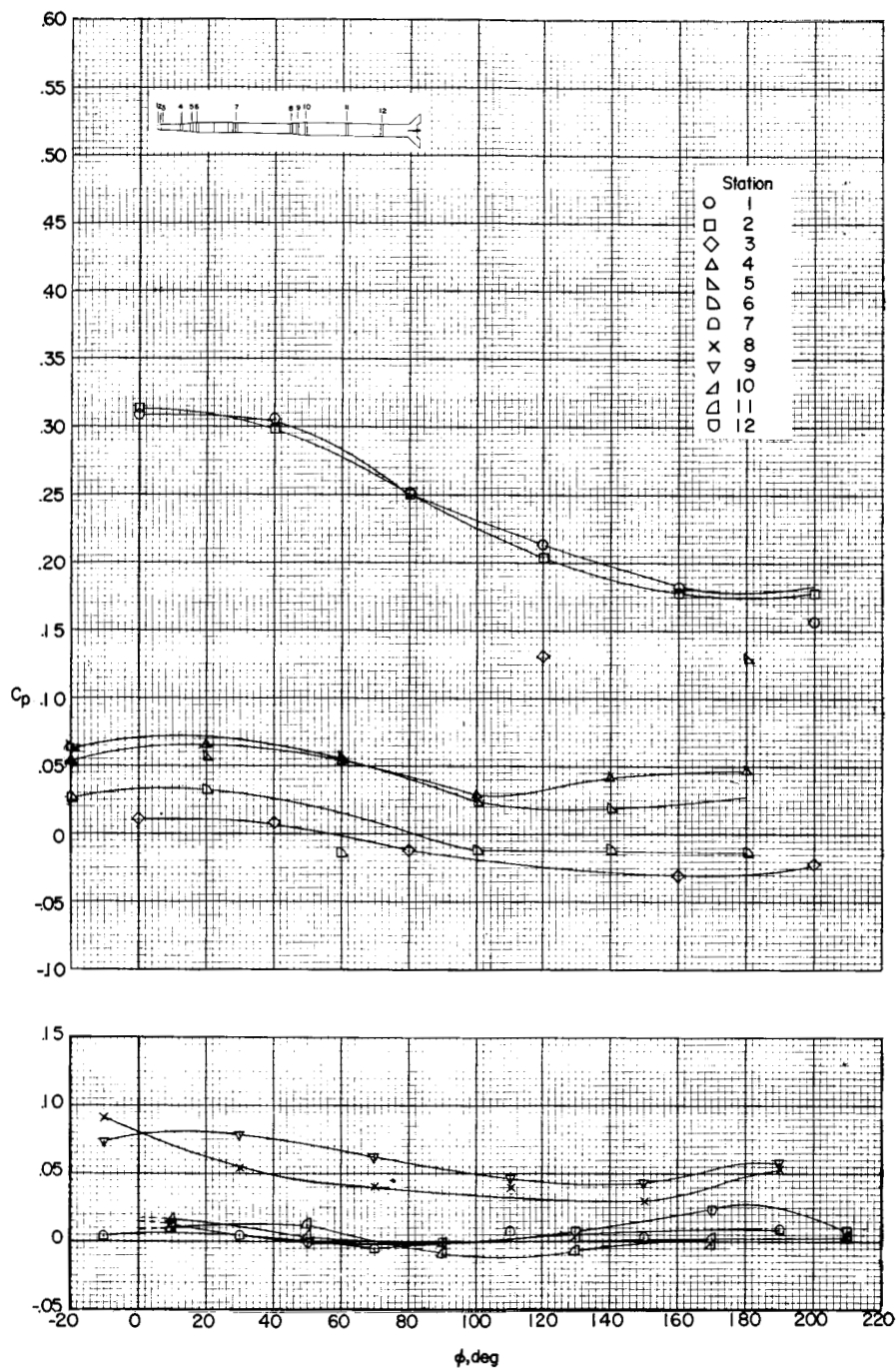
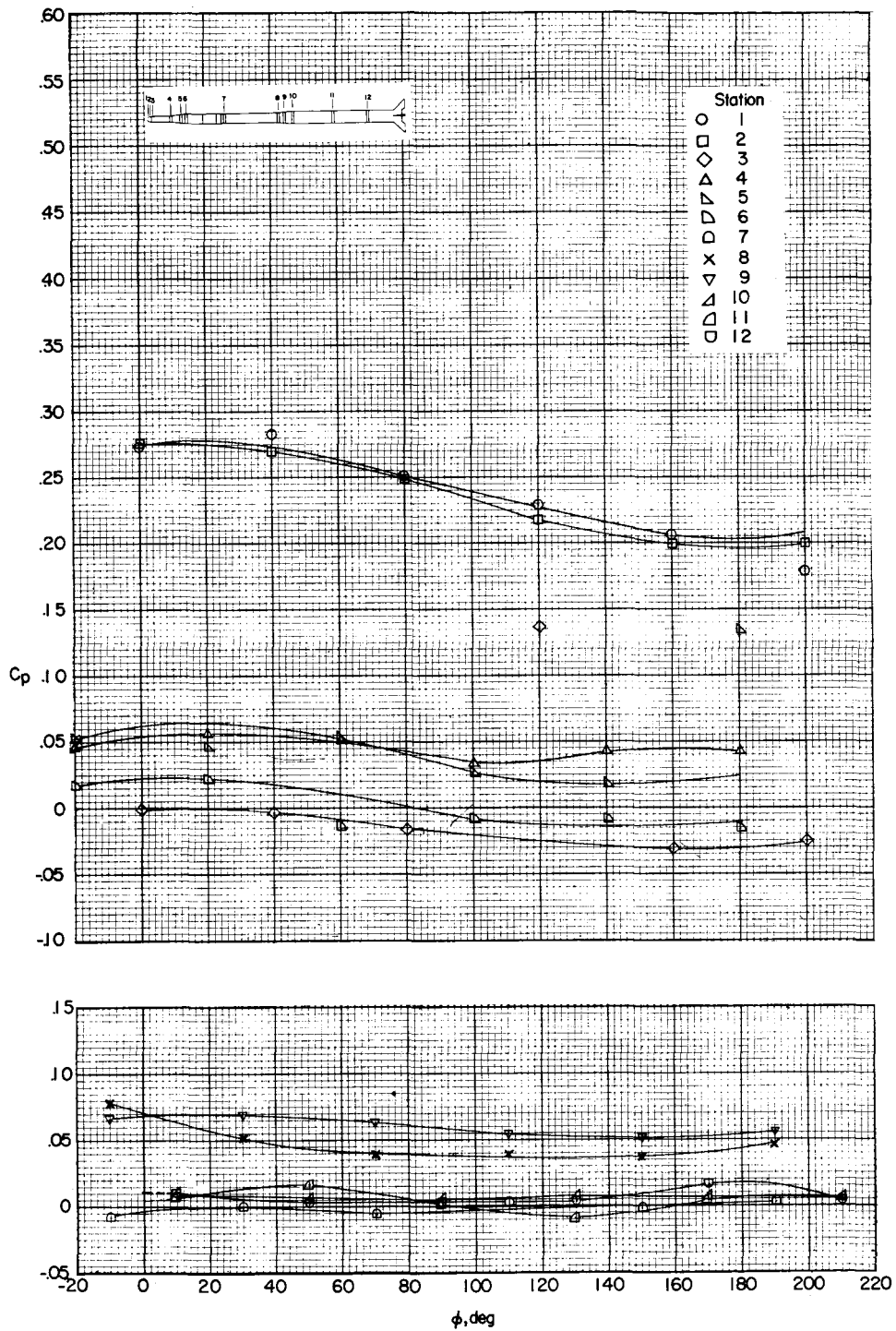


Figure 4.- Effect of body bending and fourth-stage shape on variation of C_p with x/l for $\phi = 0^\circ$ and $\alpha = 0^\circ$. Reynolds number, 2.071×10^6 based on stage 1 base diameter.



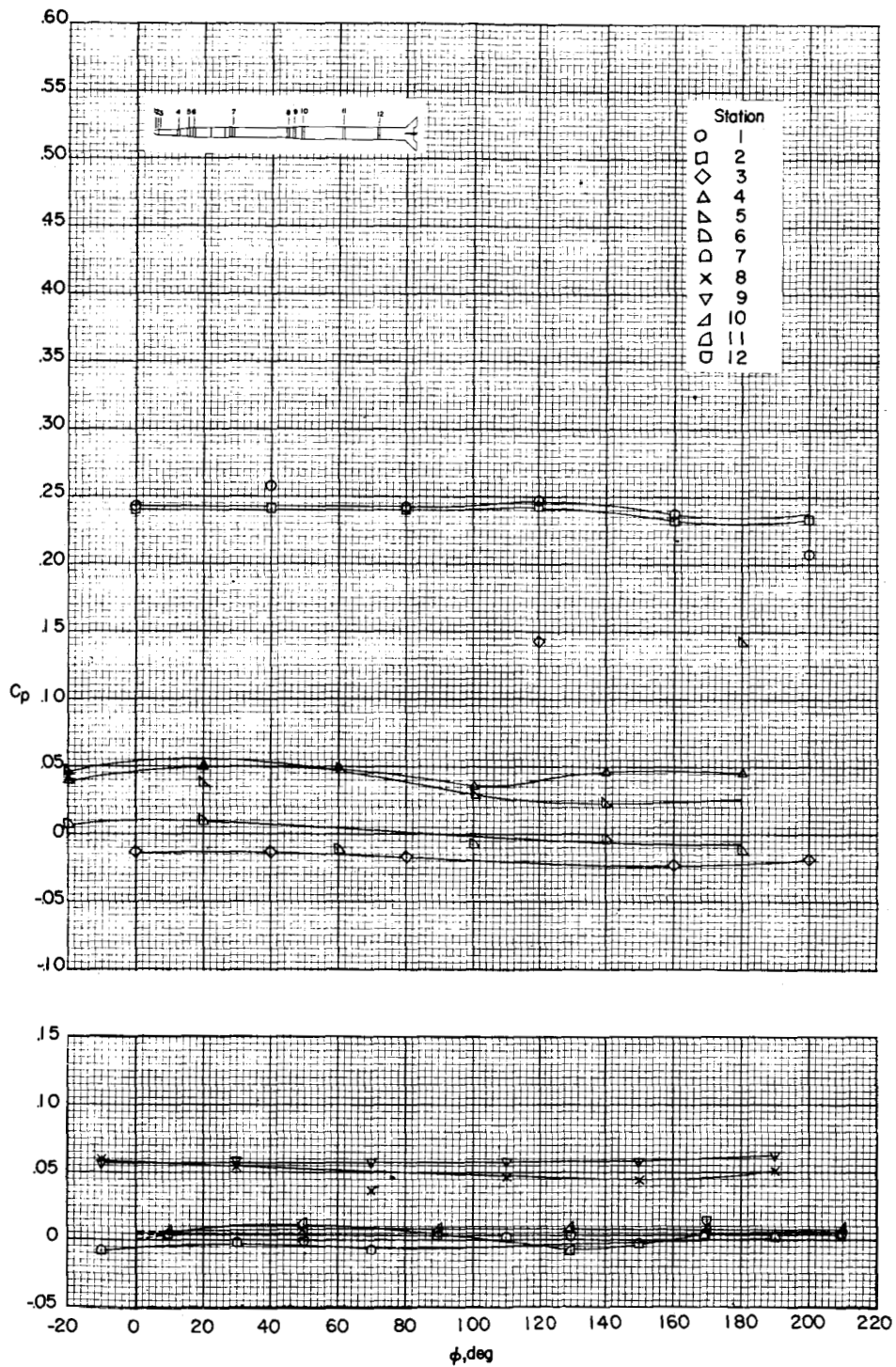
(a) $\alpha = -3.41^\circ$.

Figure 5.- Variation of C_p with ϕ for several longitudinal stations. Straight, basic fourth-stage model without base flare; Reynolds number, 2.071×10^6 based on stage 1 base diameter. (See figure 9 for pressures on base flare.)



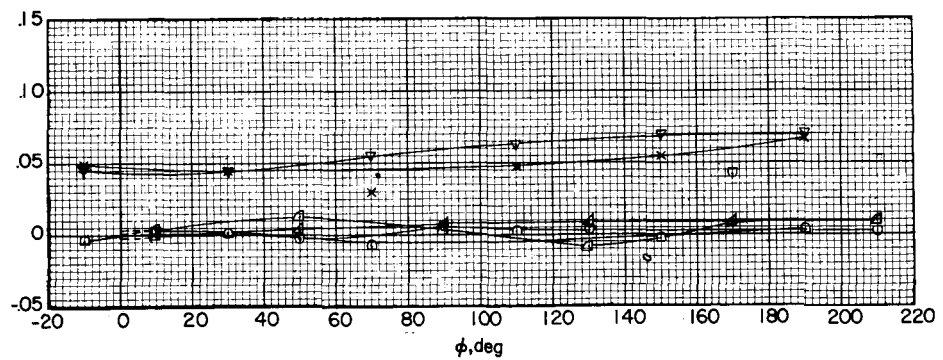
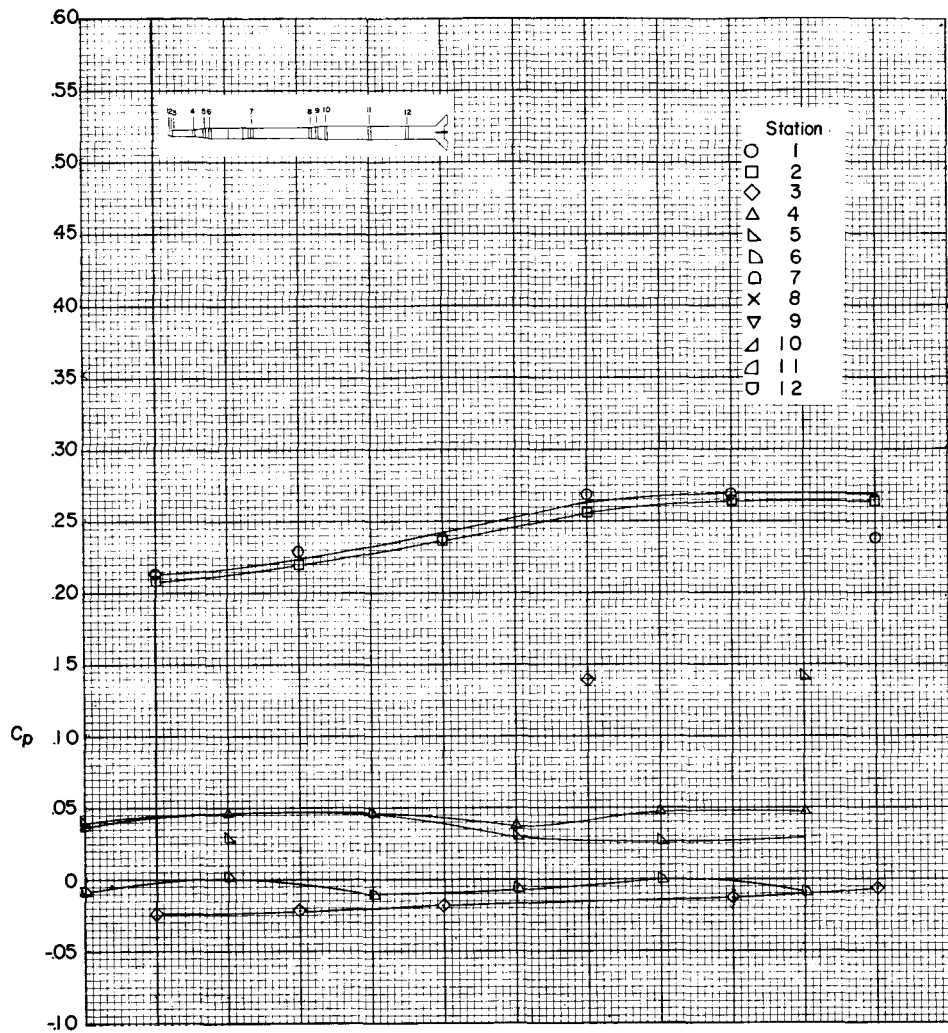
(b) $\alpha = -1.85^\circ$.

Figure 5.- Continued.



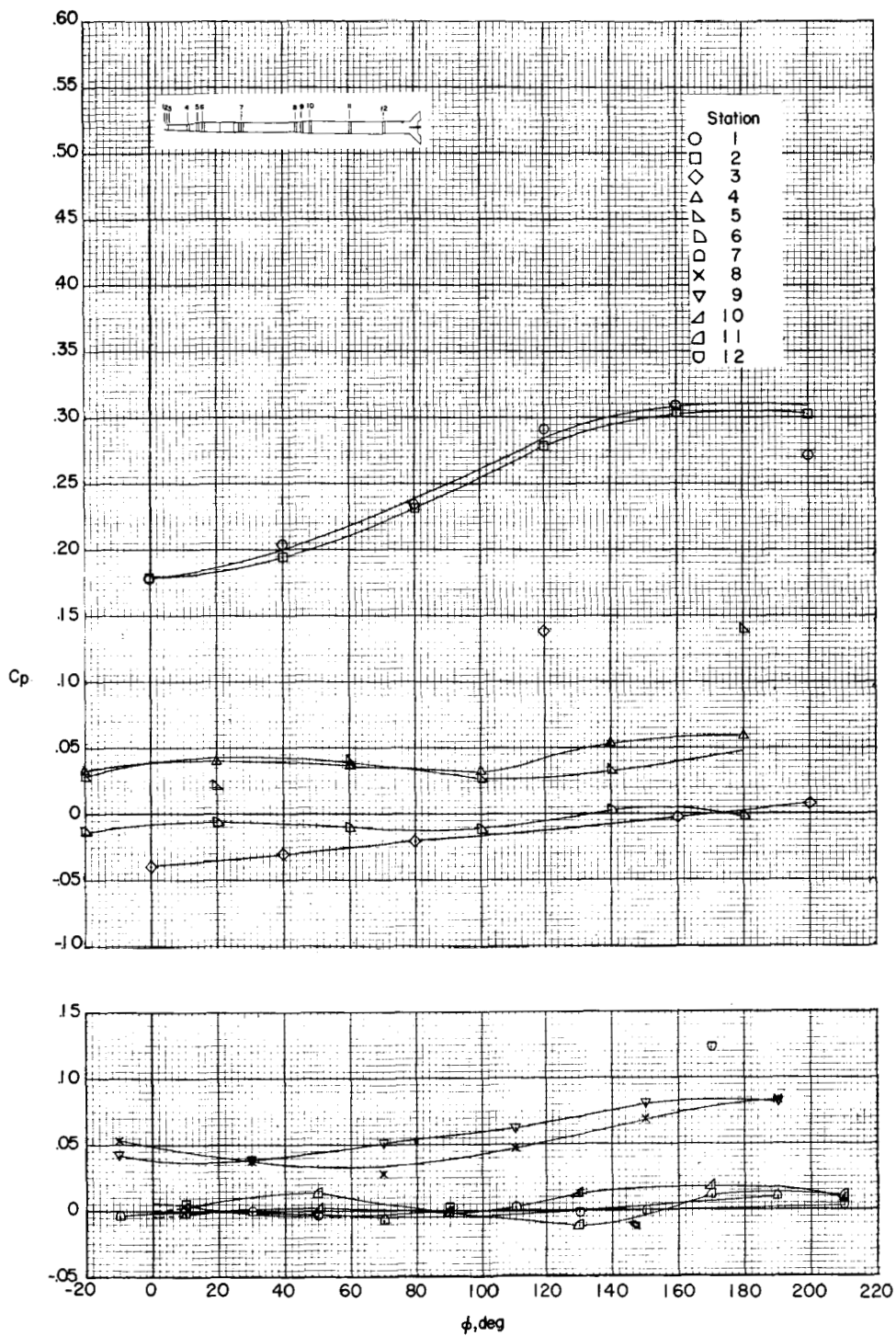
(c) $\alpha = -0.14^\circ$.

Figure 5.- Continued.



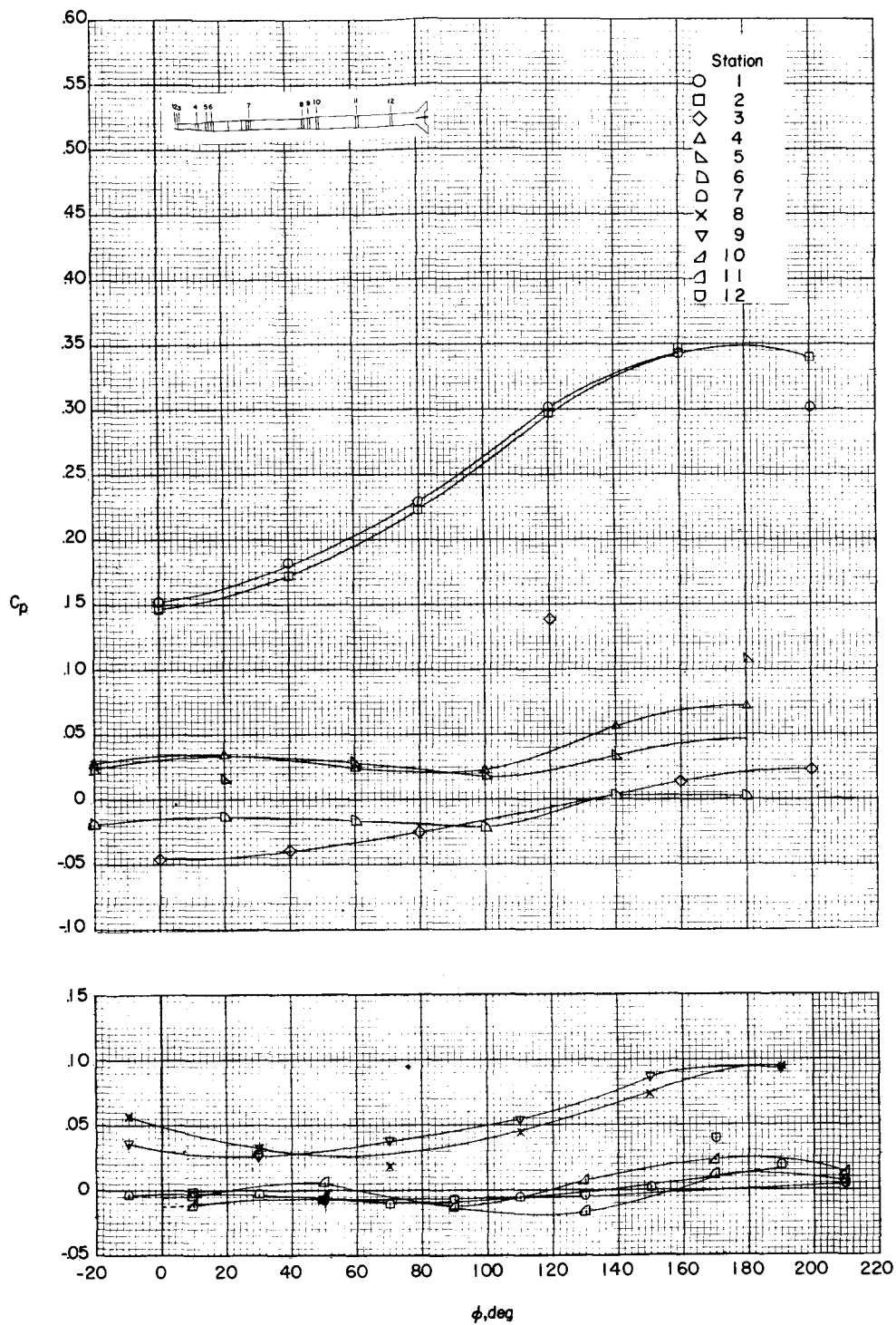
(d) $\alpha = 1.44^\circ$.

Figure 5.- Continued.



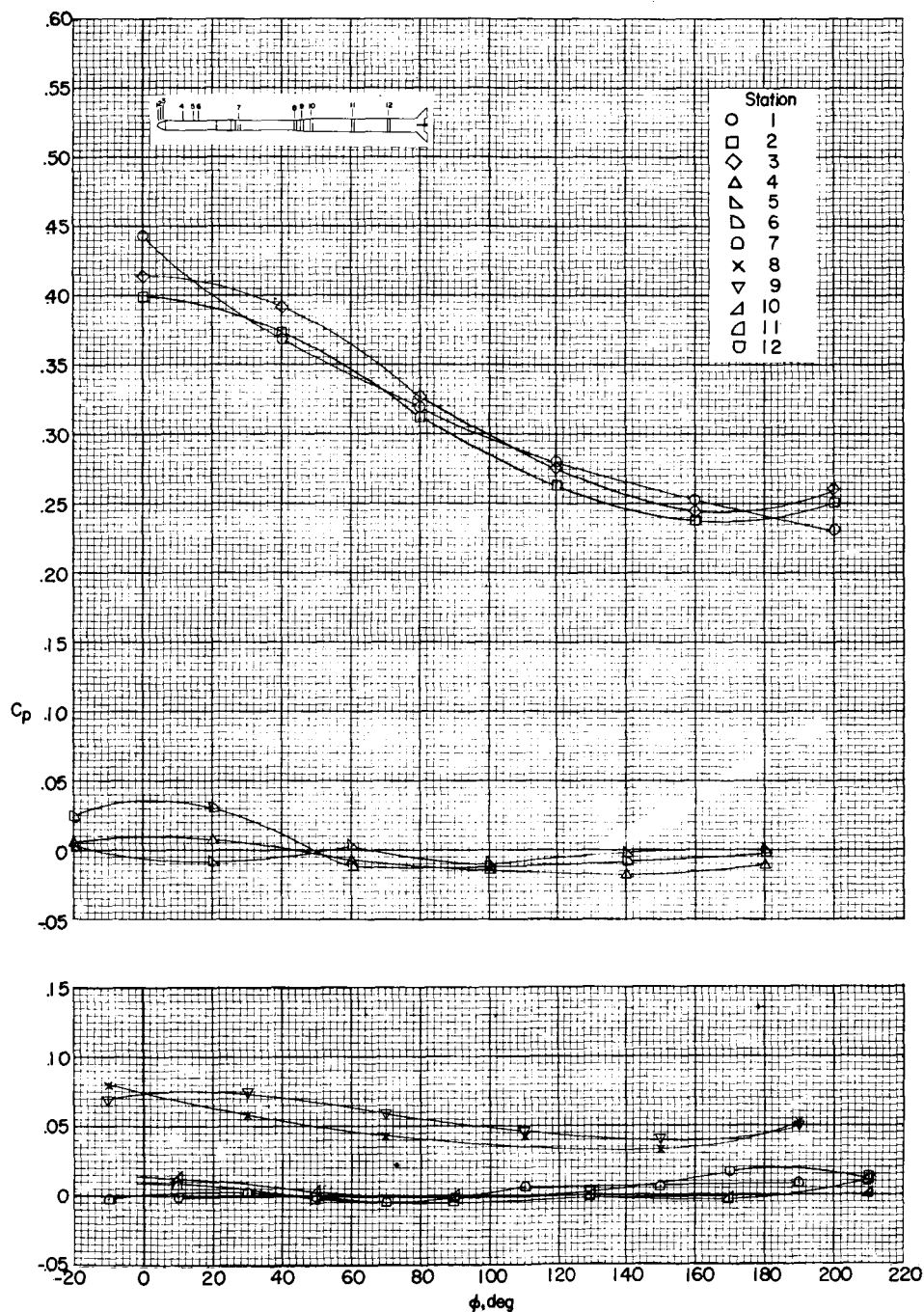
(e) $\alpha = 2.94^\circ$.

Figure 5.- Continued.



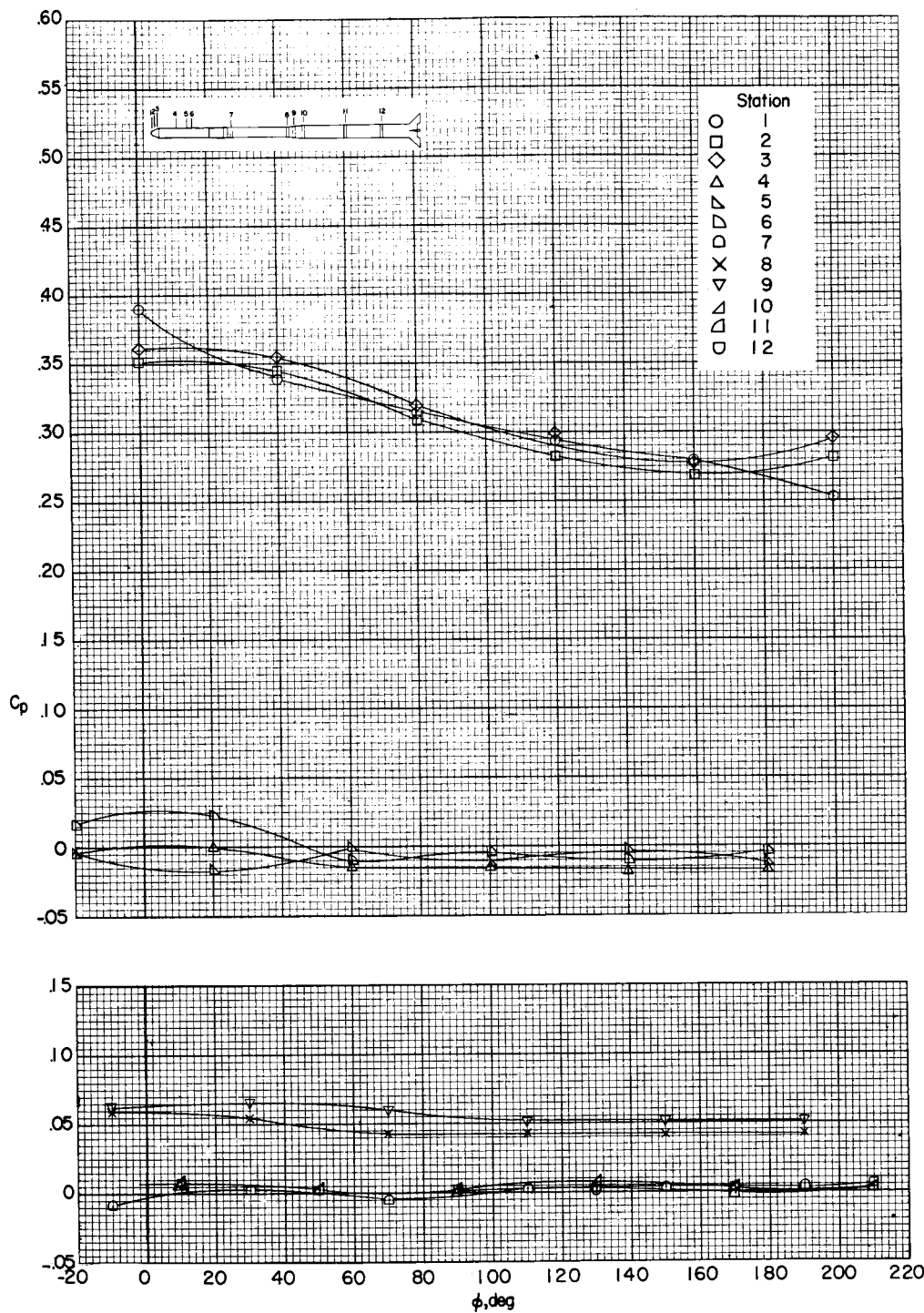
(f) $\alpha = 4.57^\circ$.

Figure 5.- Concluded.



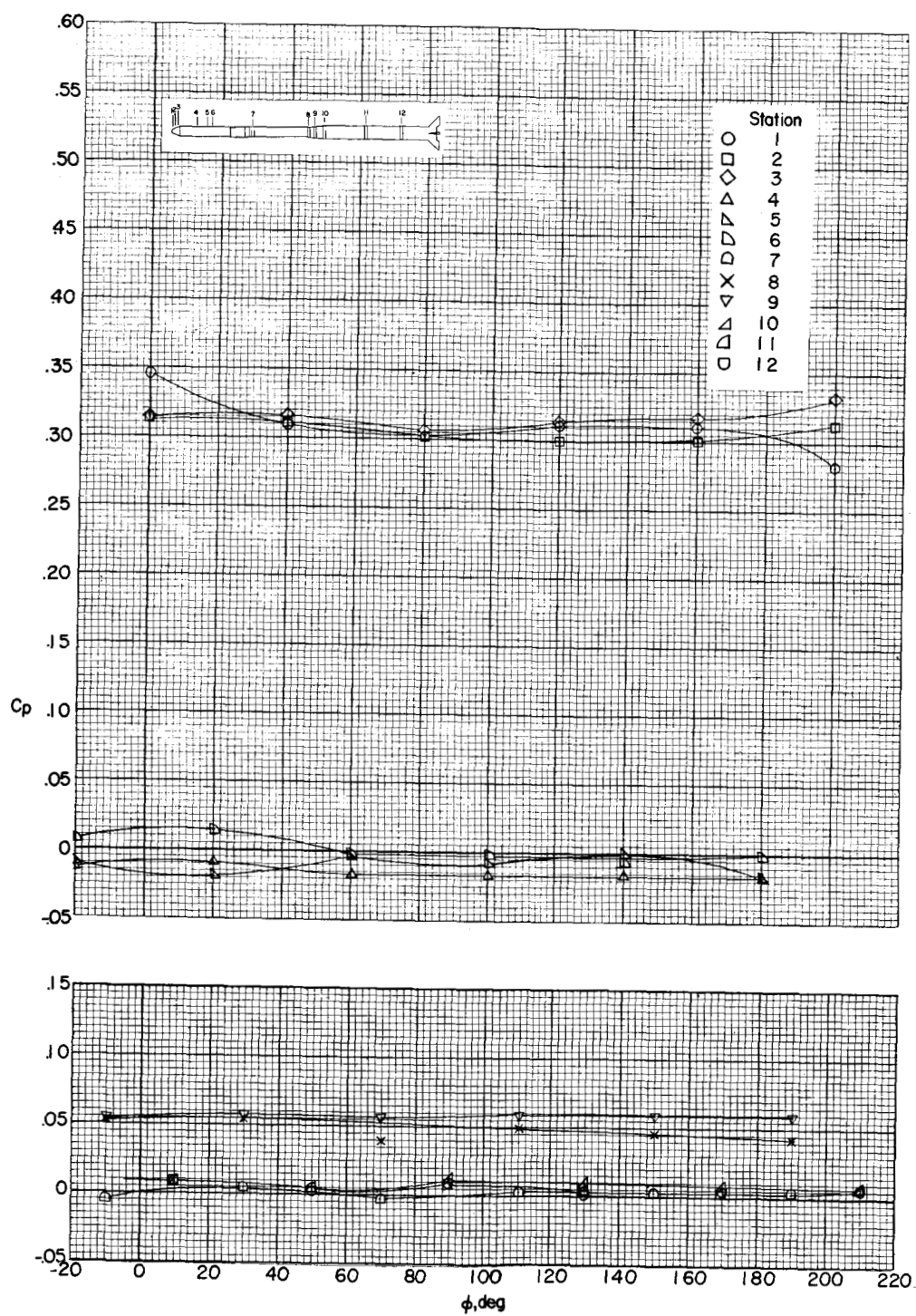
(a) $\alpha = -3.40^\circ$.

Figure 6.- Variation of C_p with ϕ for several longitudinal stations. Straight, enlarged fourth-stage model without base flare; Reynolds number, 2.071×10^6 based on stage 1 base diameter. (See figure 10 for pressures on base flare.)



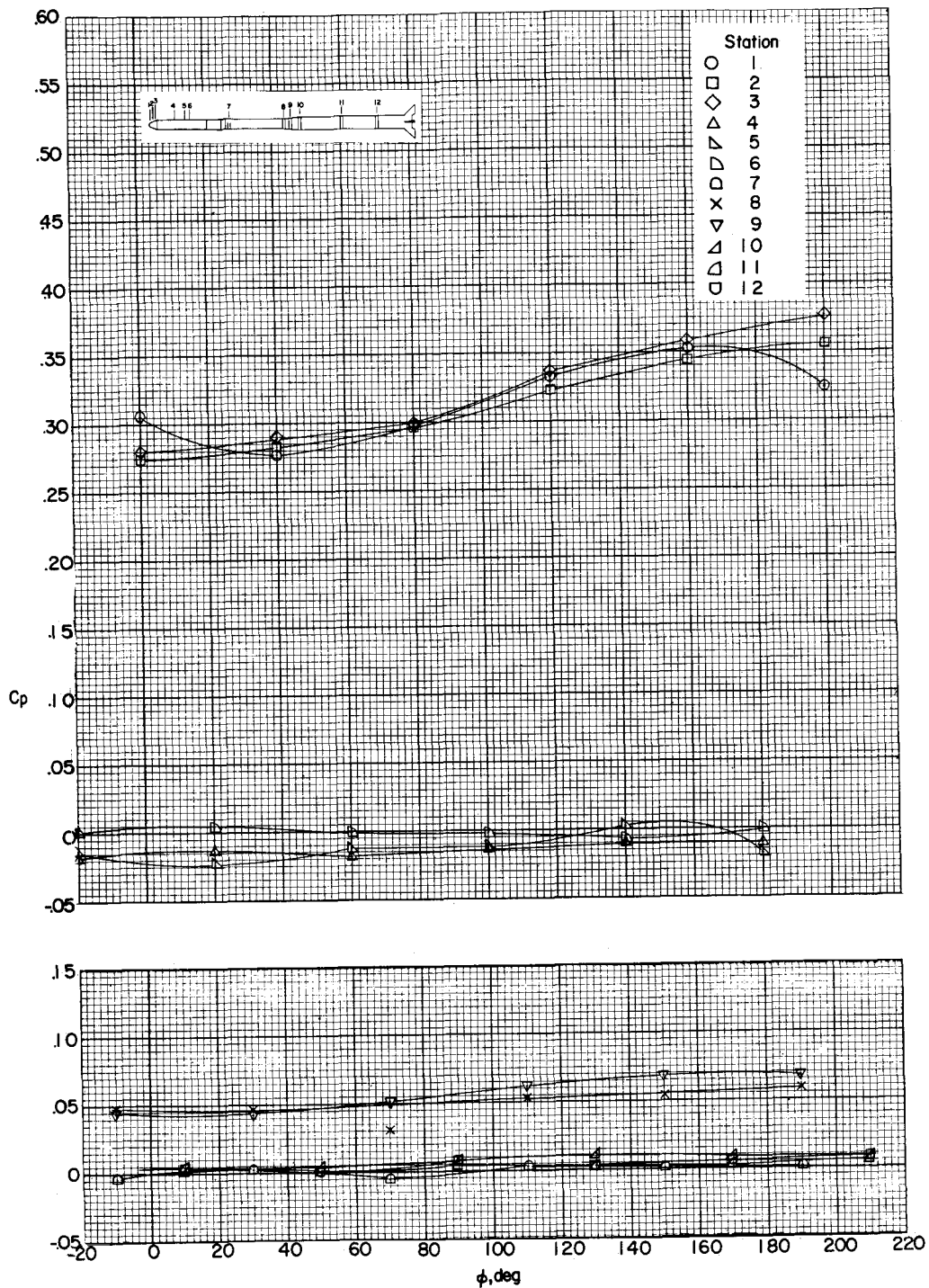
(b) $\alpha = -1.42^\circ$.

Figure 6.- Continued.



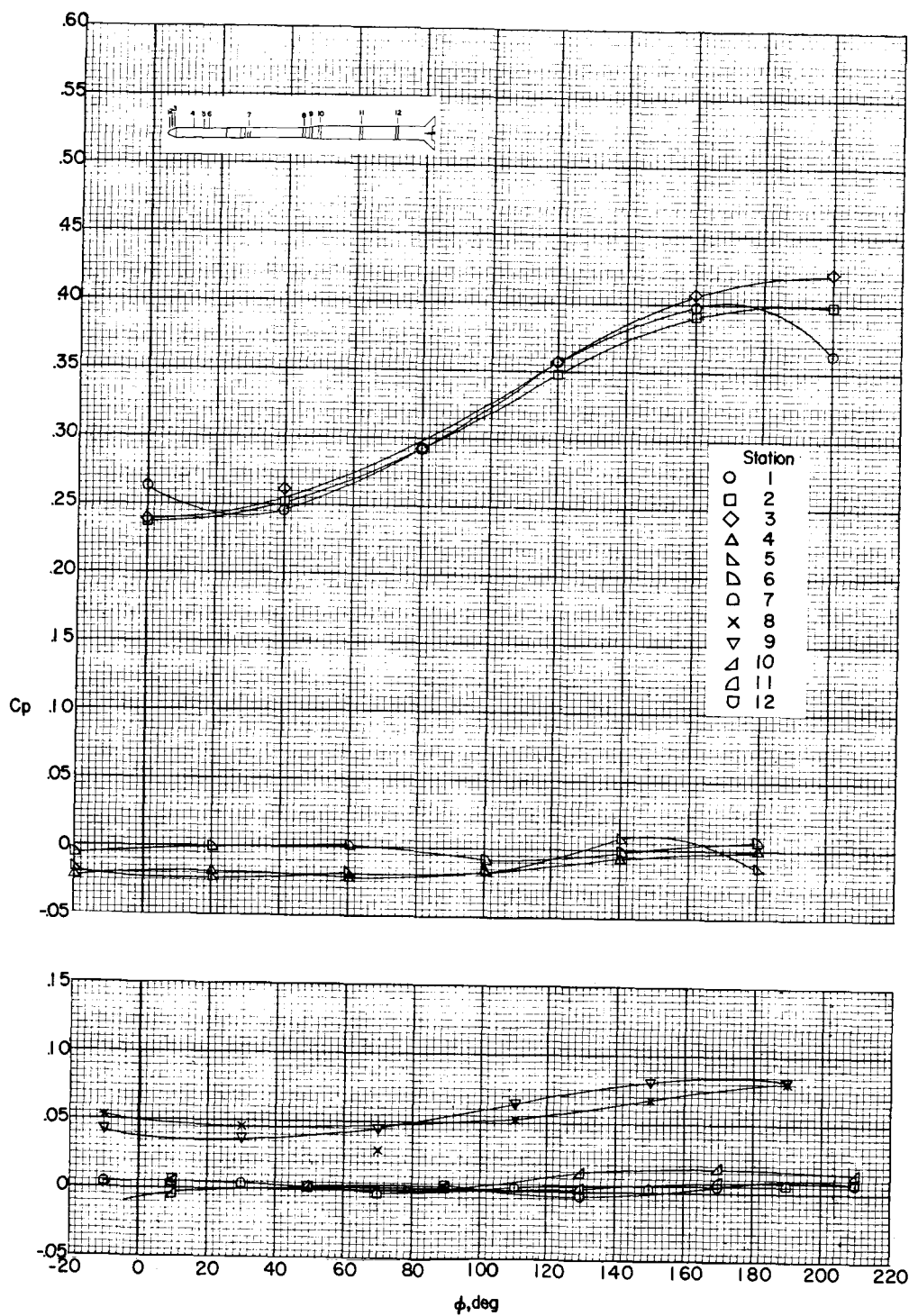
(c) $\alpha = 0.01^\circ$.

Figure 6.- Continued.



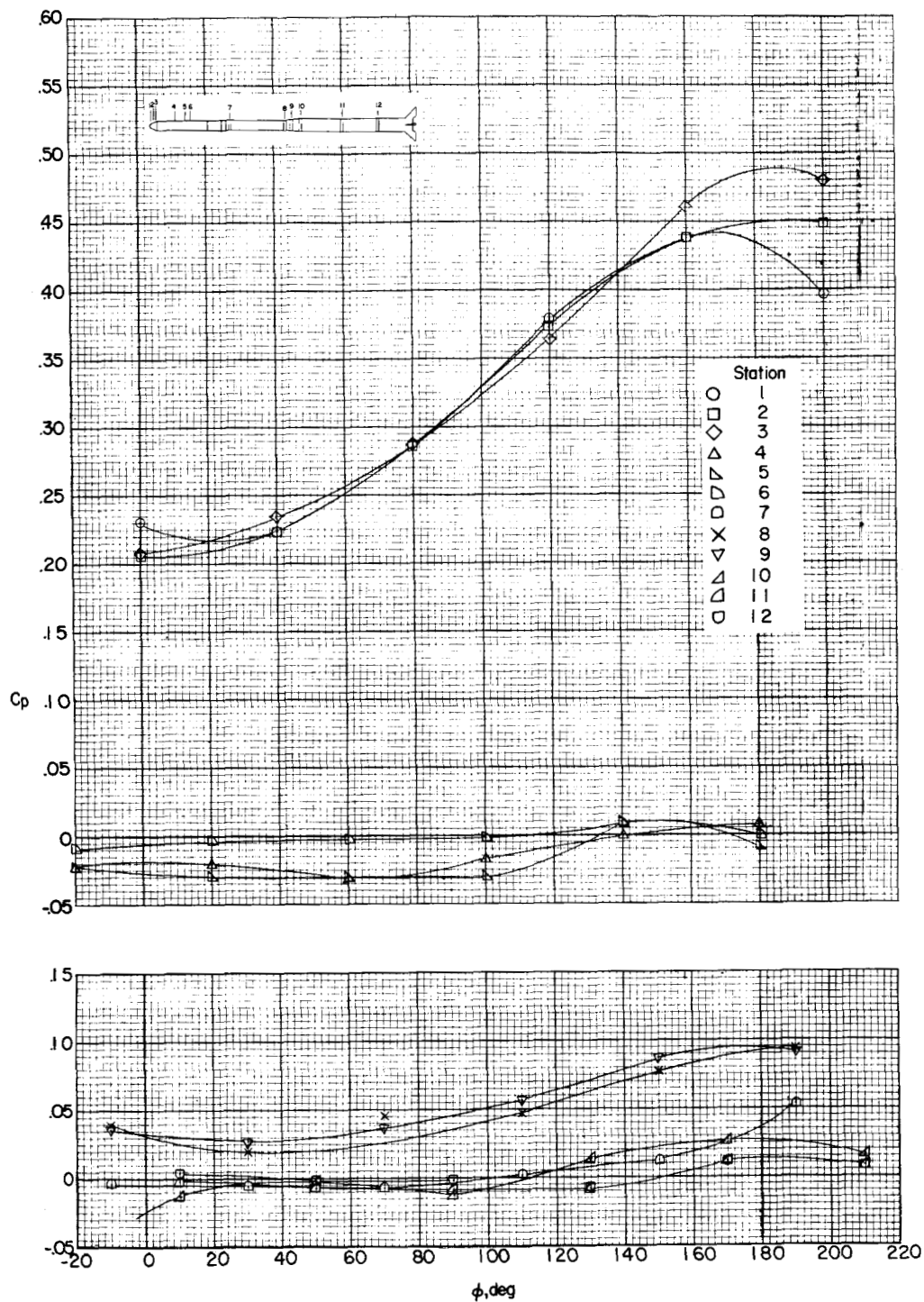
(d) $\alpha = 1.65^\circ$.

Figure 6.- Continued.



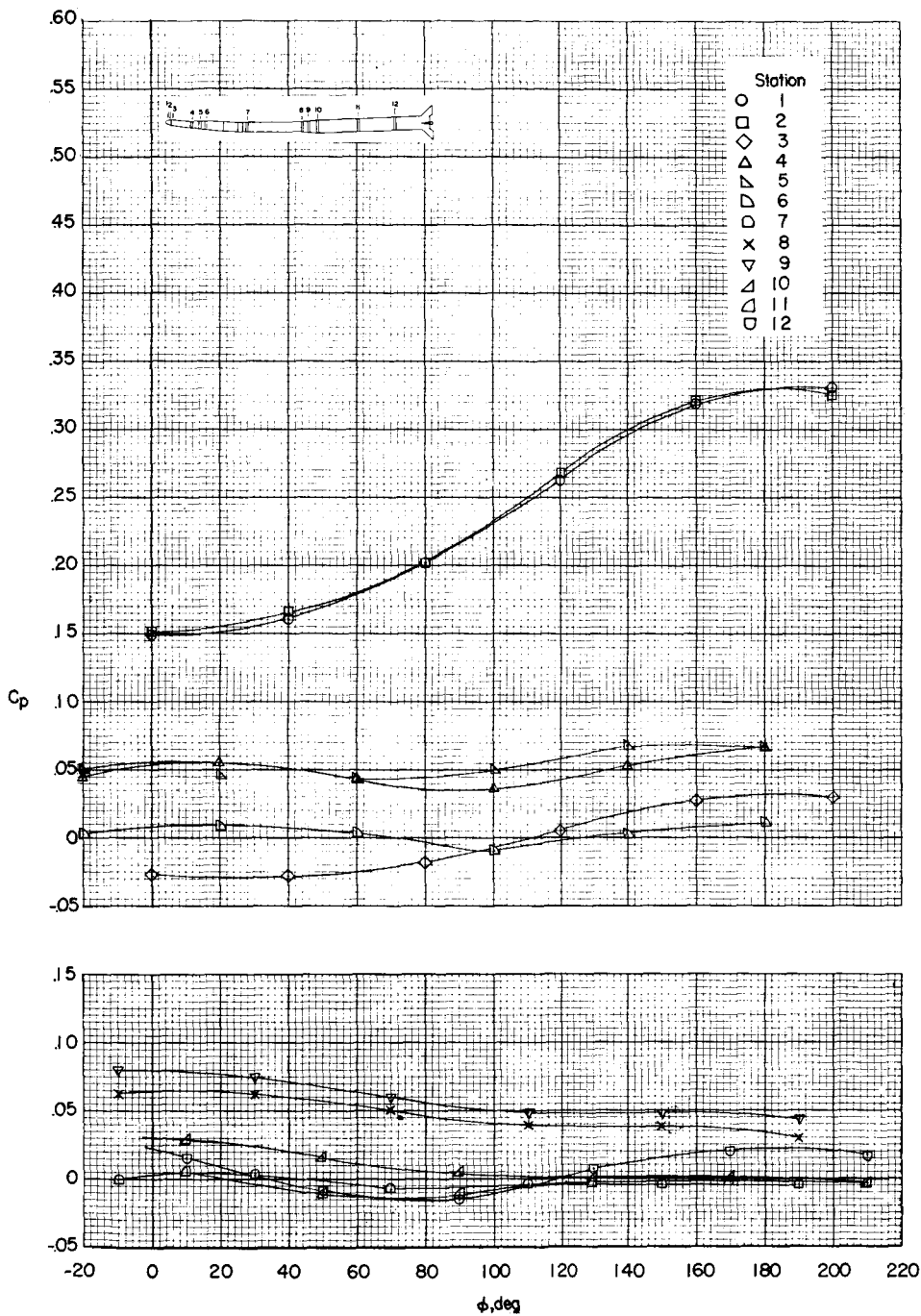
(e) $\alpha = 3.15^\circ$.

Figure 6.- Continued.



(f) $\alpha = 4.79^\circ$.

Figure 6.- Concluded.



(a) $\alpha = -3.53^\circ$.

Figure 7.- Variation of C_p with ϕ for several longitudinal stations. Bent, basic fourth-stage model without base flare; Reynolds number, 2.071×10^6 based on stage 1 base diameter. (See figure 11 for pressures on base flare.)

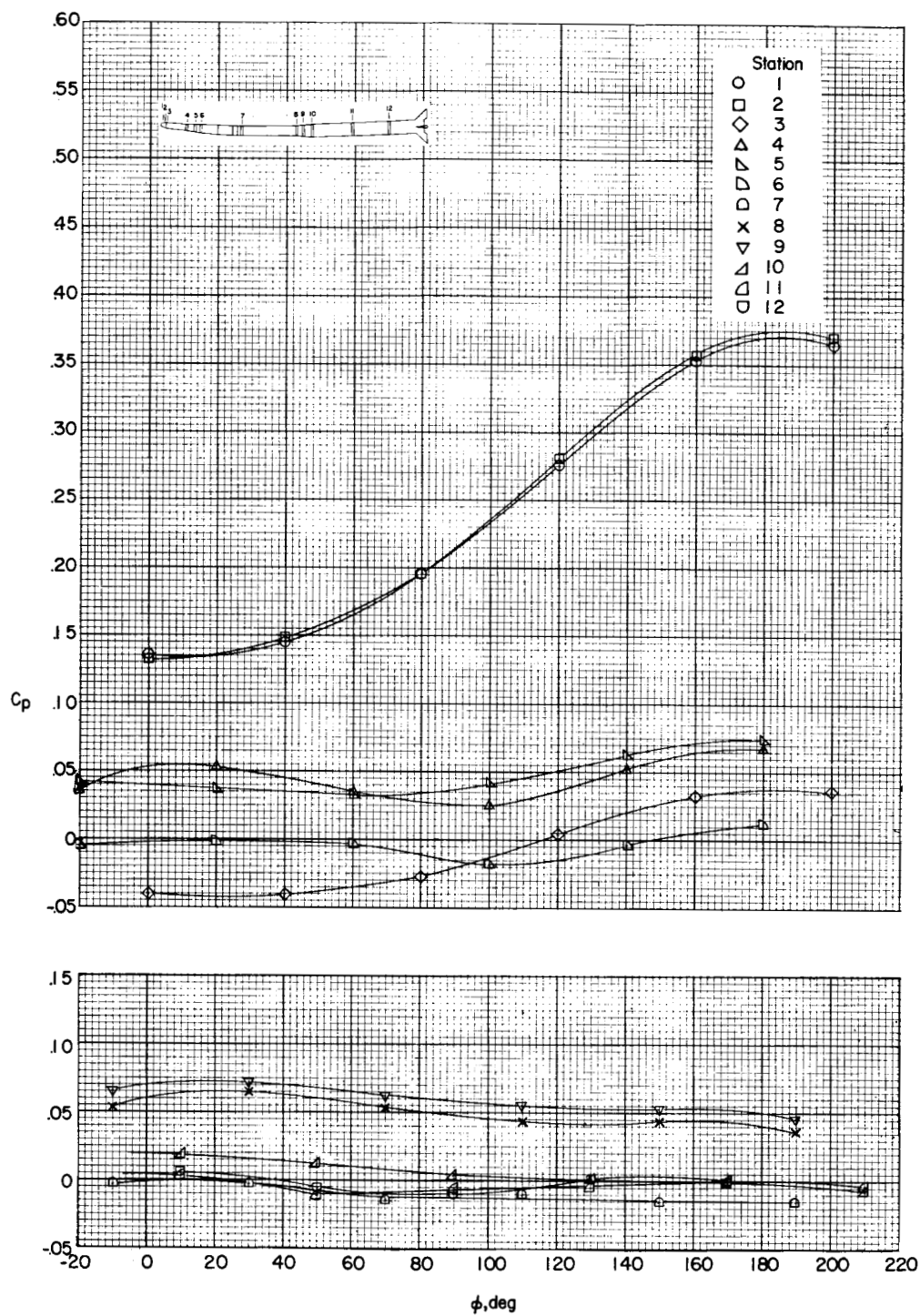
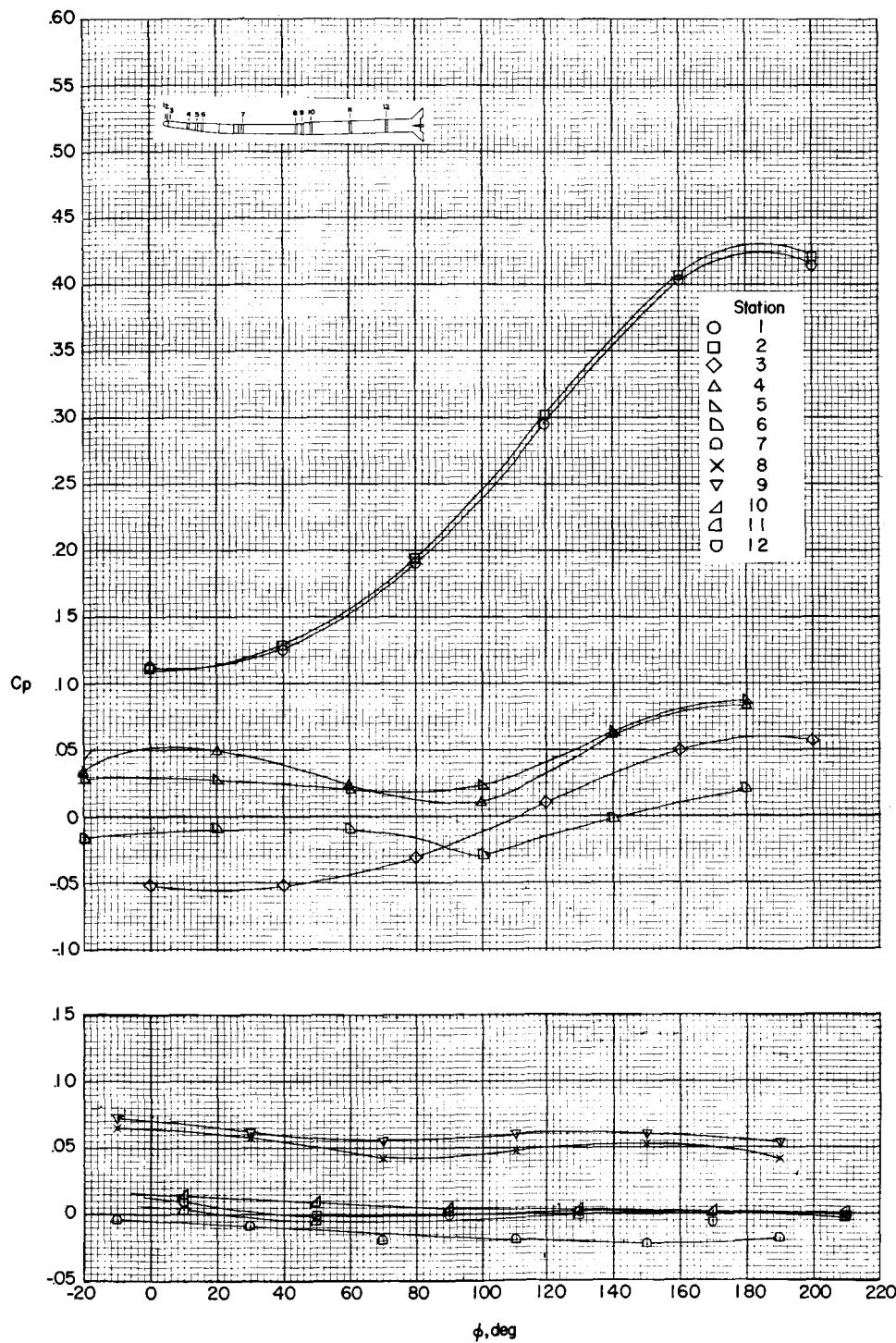
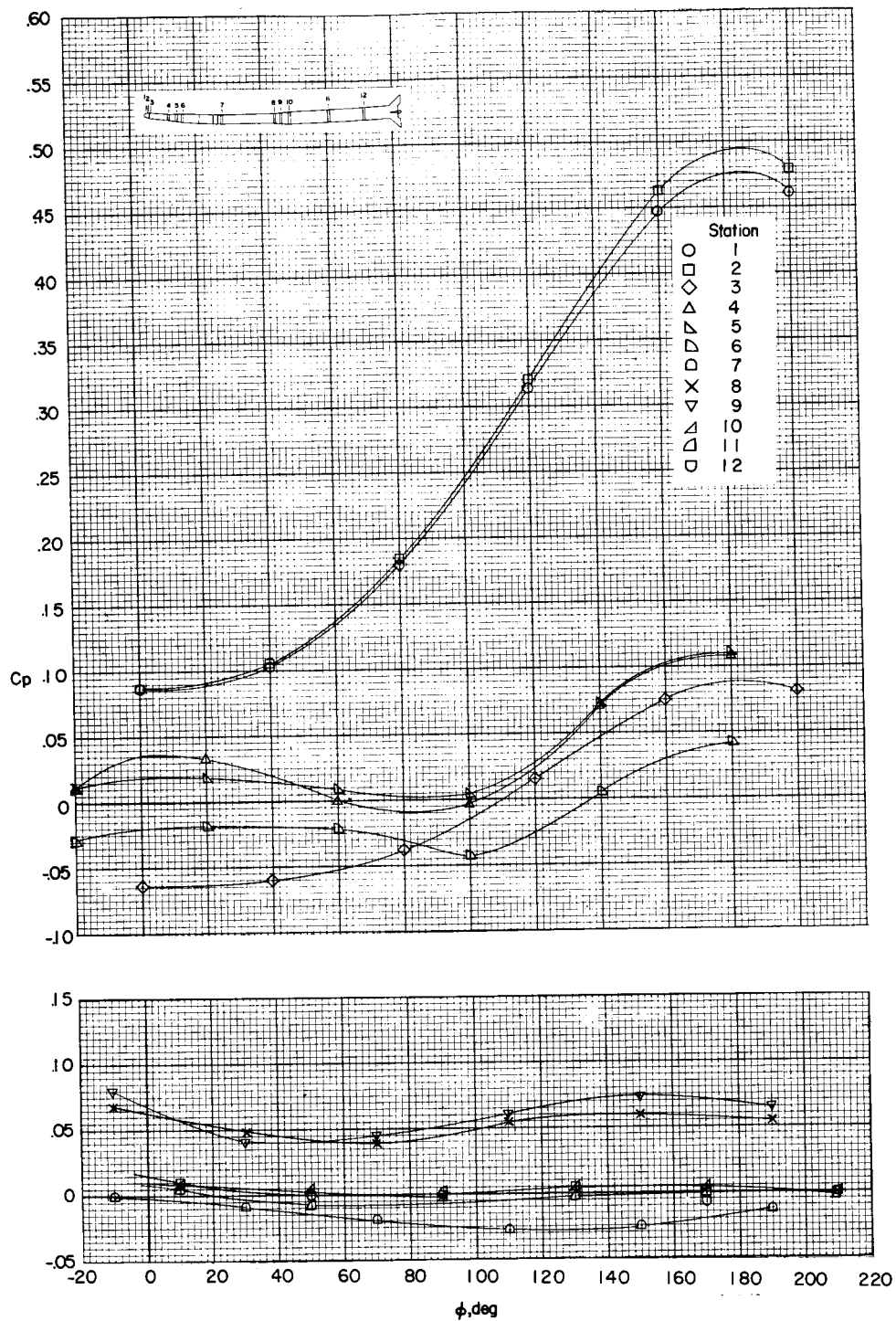


Figure 7.- Continued.



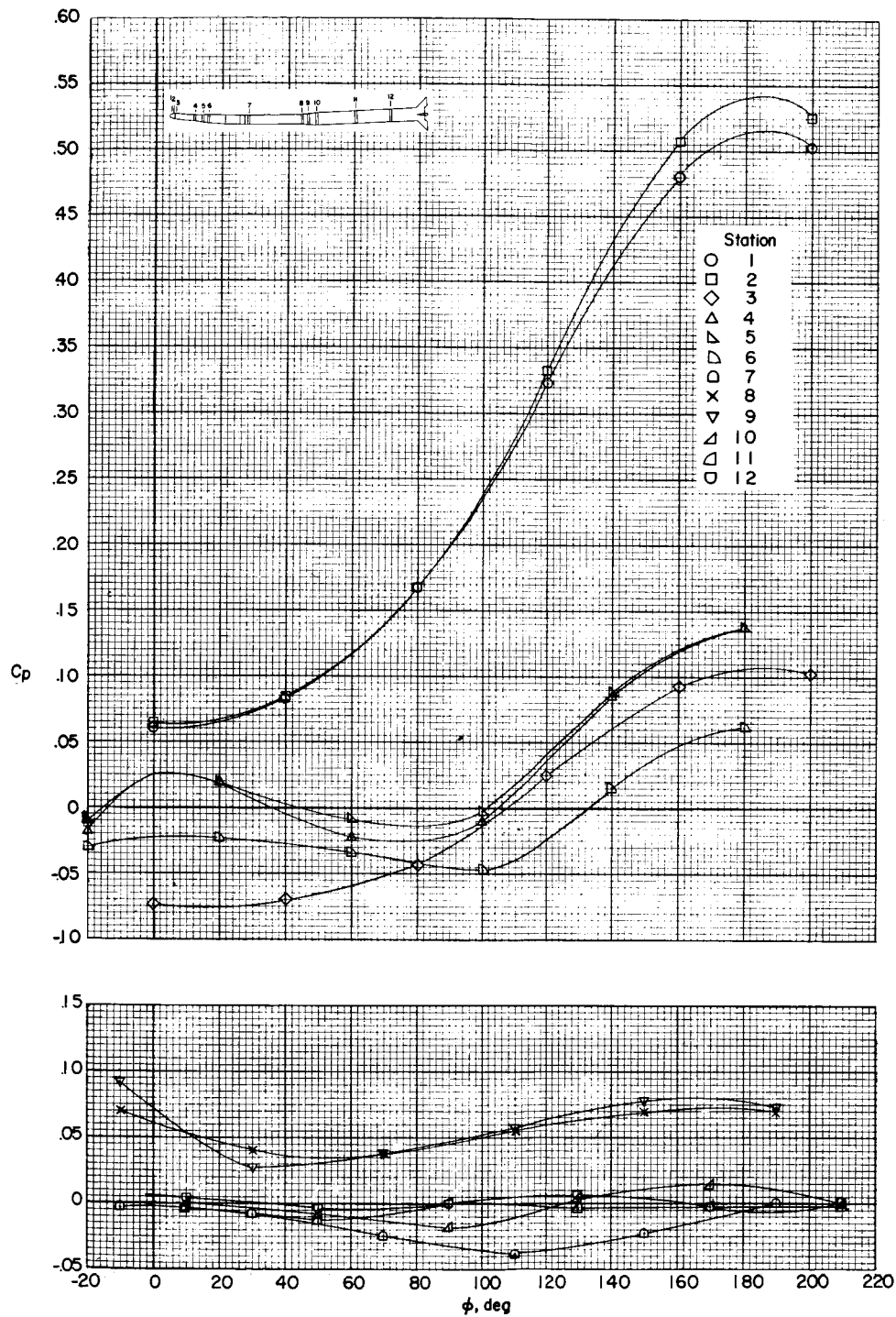
(c) $\alpha = 0.11^\circ$.

Figure 7.- Continued.



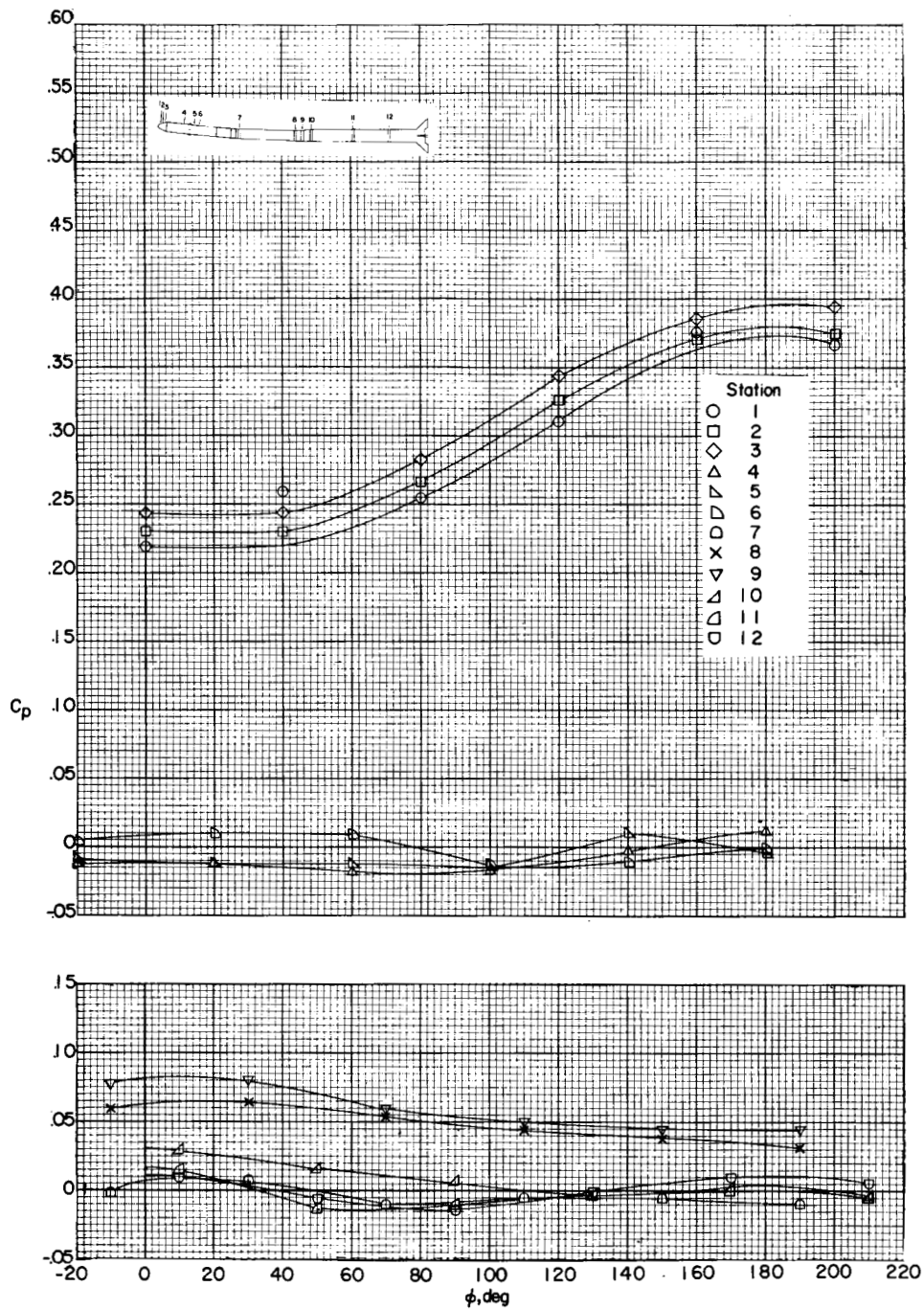
(d) $\alpha = 1.54^\circ$.

Figure 7.- Continued.



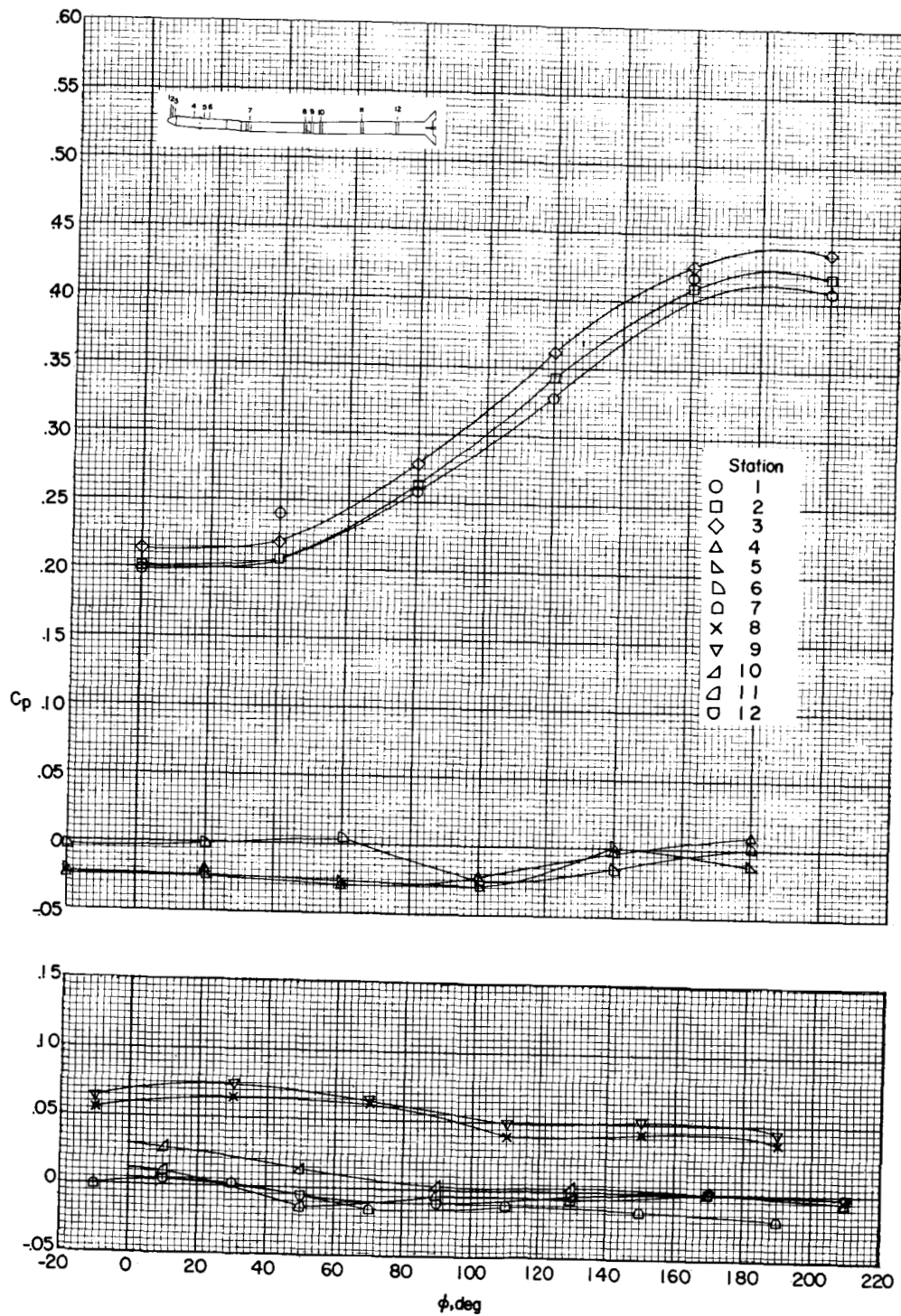
(e) $\alpha = 3.39^\circ$.

Figure 7.- Concluded.



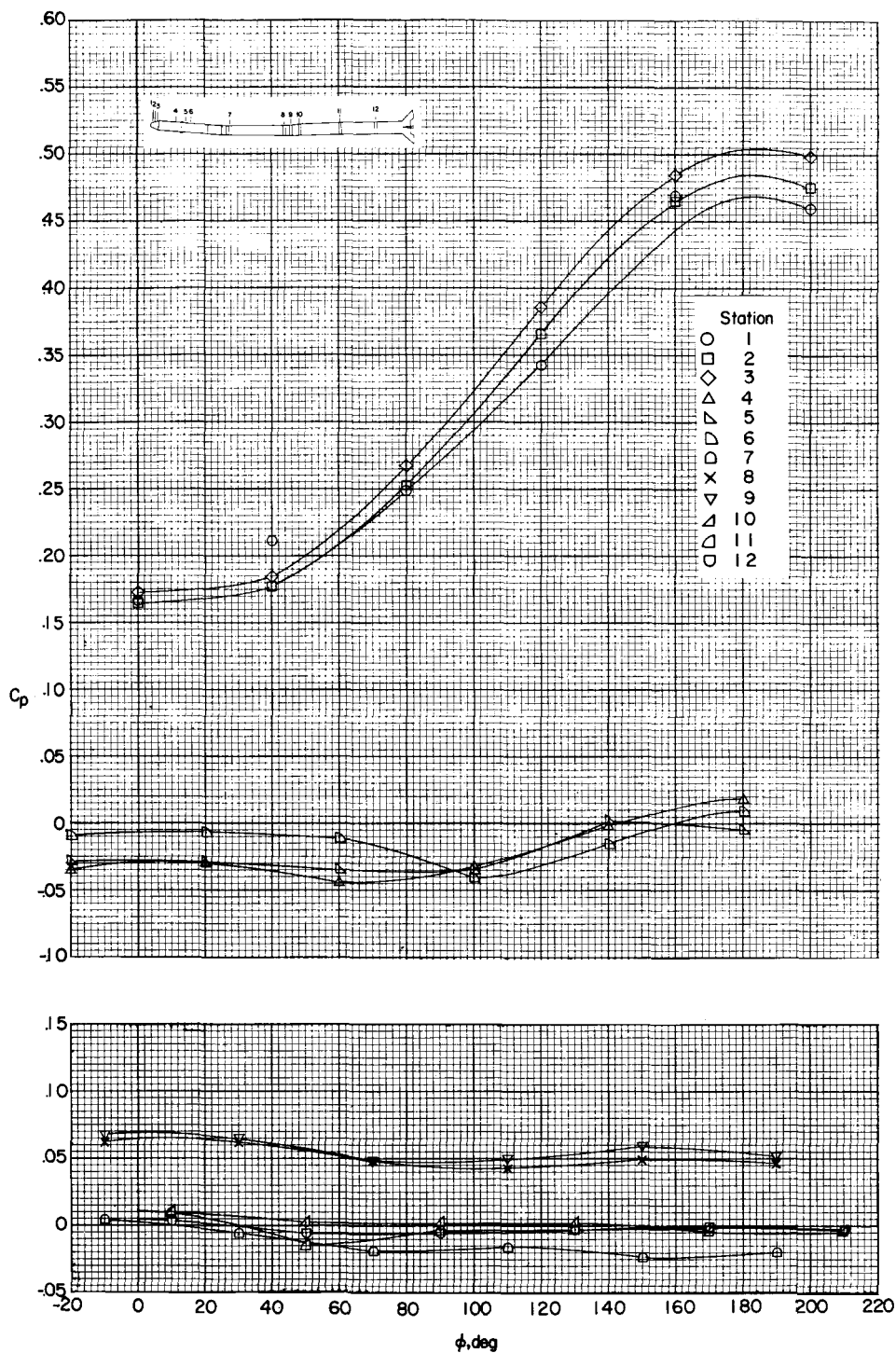
(a) $\alpha = -3.22^\circ$.

Figure 8.- Variation of C_p with ϕ for several longitudinal stations. Bent, enlarged fourth-stage model without base flare; Reynolds number, 2.071×10^6 based on stage 1 base diameter. (See figure 12 for pressures on base flare.)



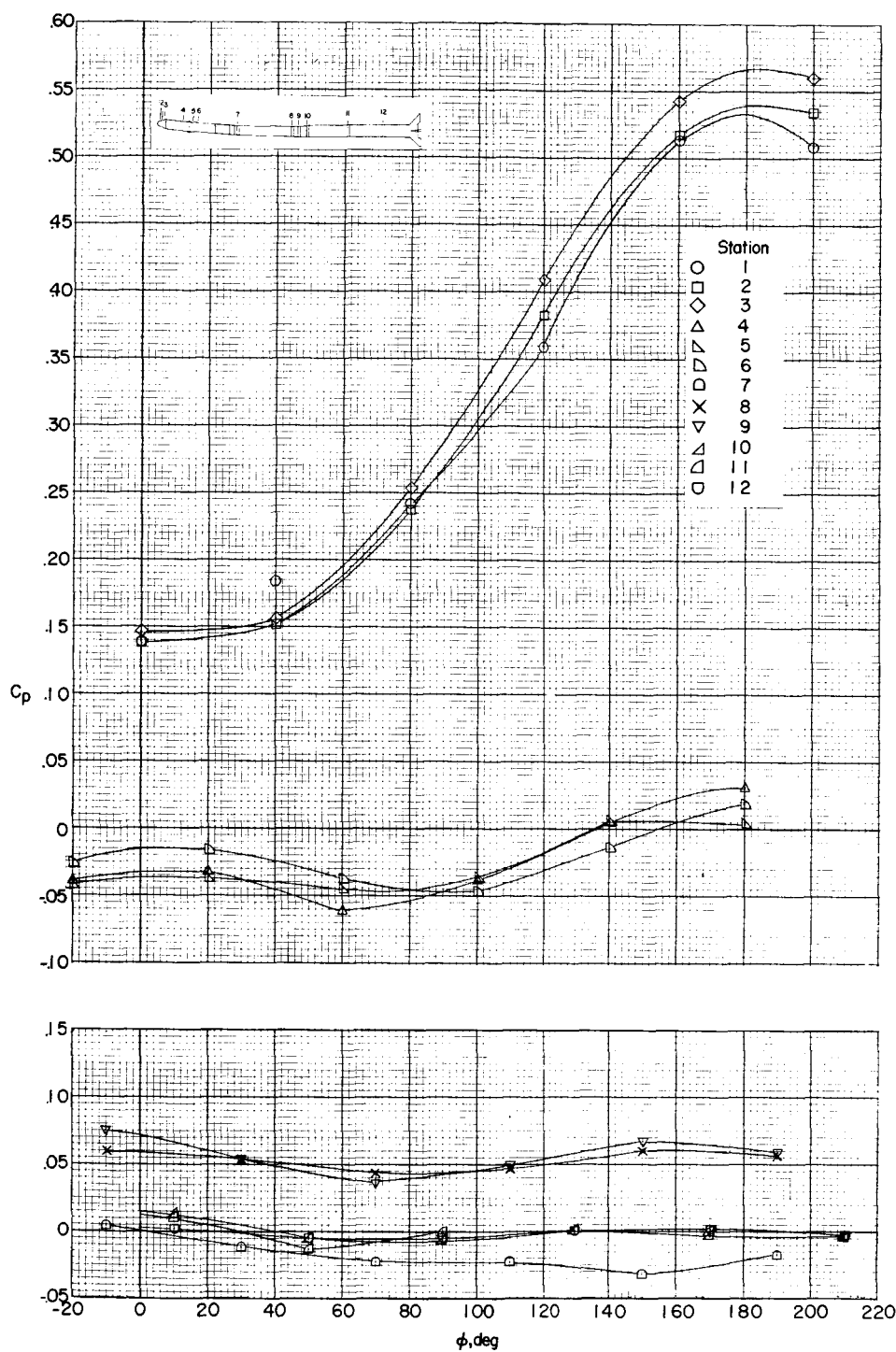
(b) $\alpha = -1.58^\circ$.

Figure 8.- Continued.



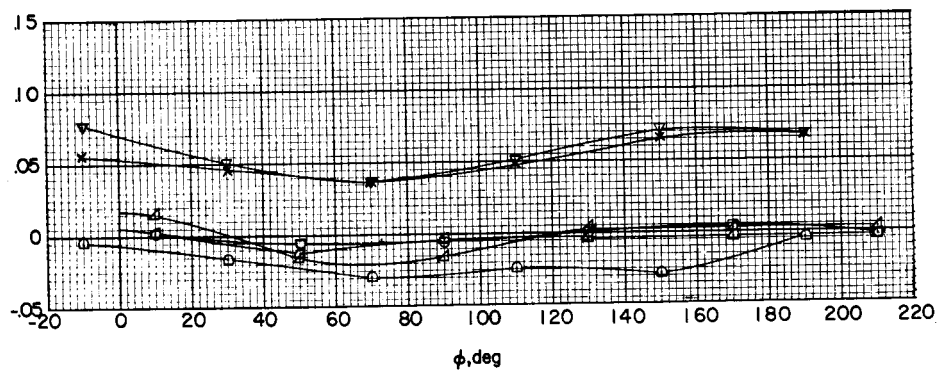
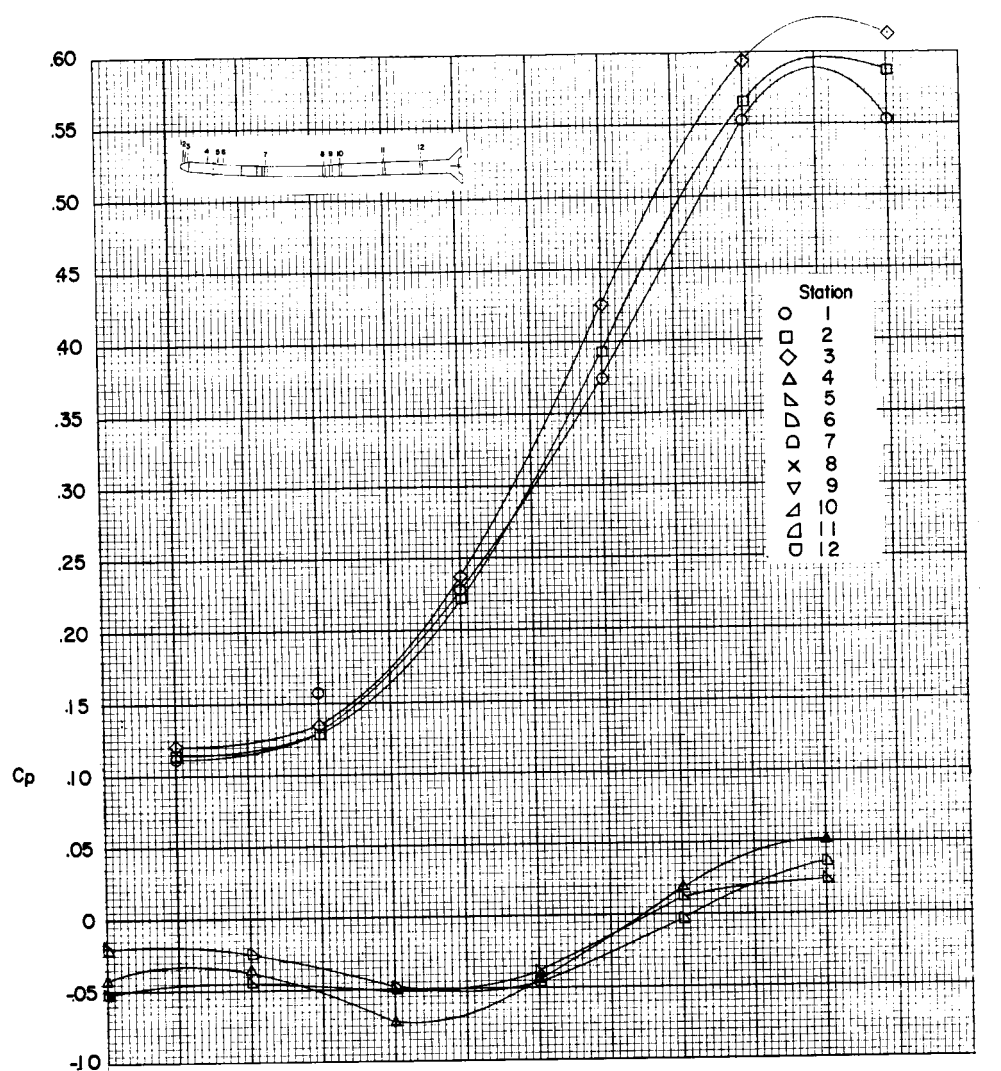
(c) $\alpha = 0.27^\circ$.

Figure 8.- Continued.



(d) $\alpha = 1.77^\circ$.

Figure 8.- Continued.



(e) $\alpha = 3.42^\circ$.

Figure 8.- Concluded.

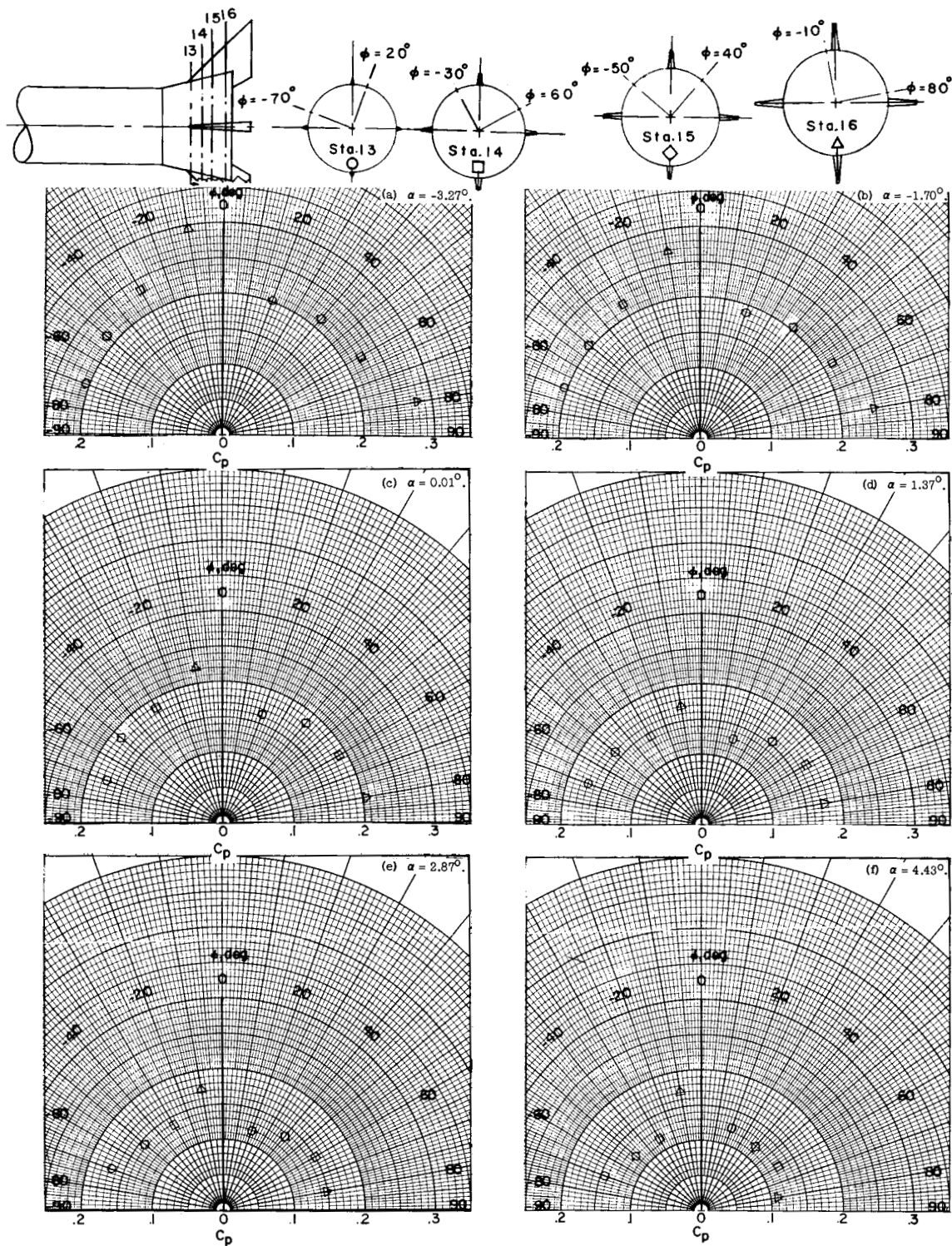


Figure 9.- Variation of C_p with ϕ for four longitudinal stations on a 13° base flare. Straight, basic fourth-stage model; Reynolds number, 2.071×10^6 based on stage 1 base diameter.

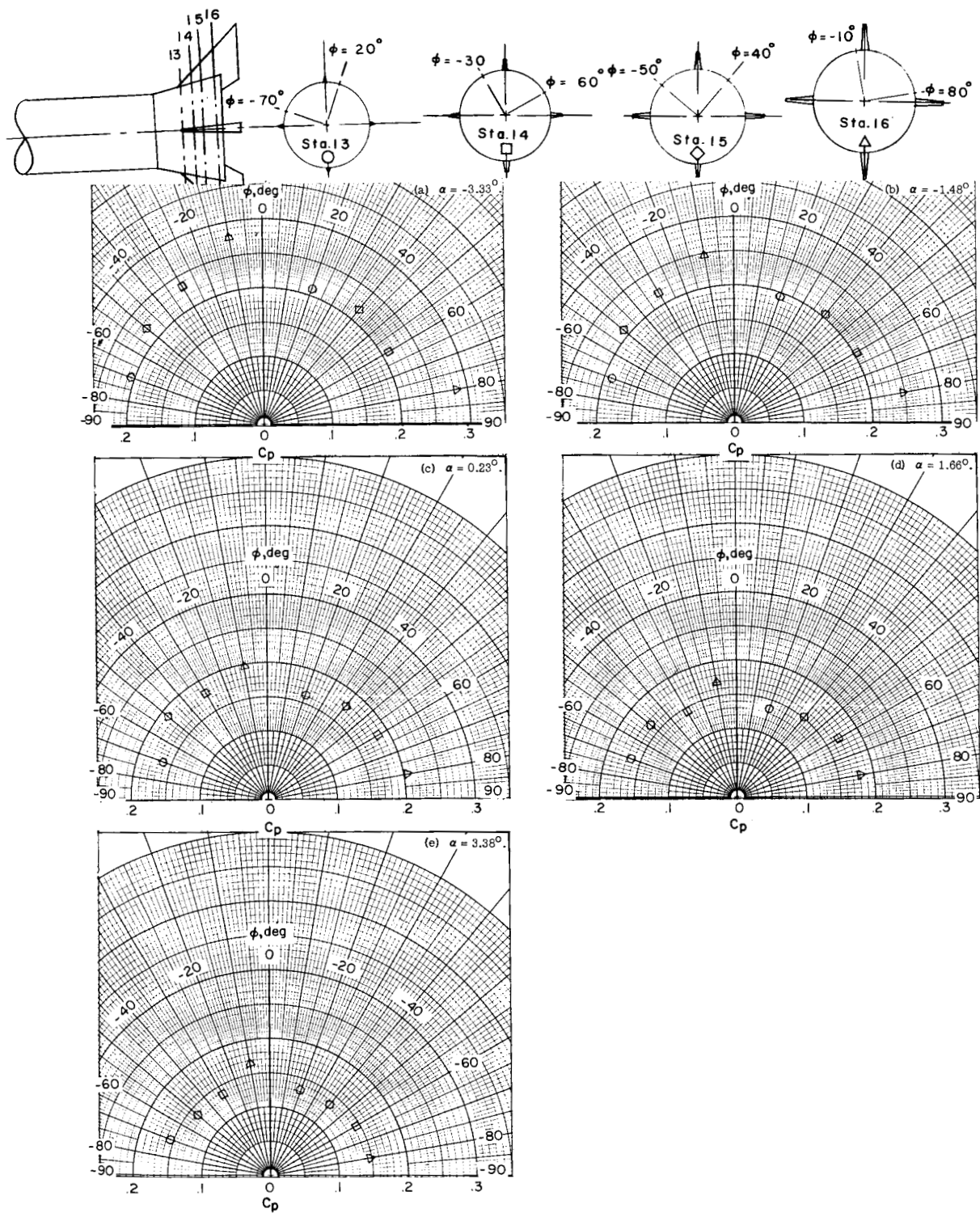


Figure 10.- Variation of C_p with ϕ for four longitudinal stations on a 13° base flare. Straight, enlarged fourth-stage model; Reynolds number, 2.071×10^6 based on stage 1 base diameter.

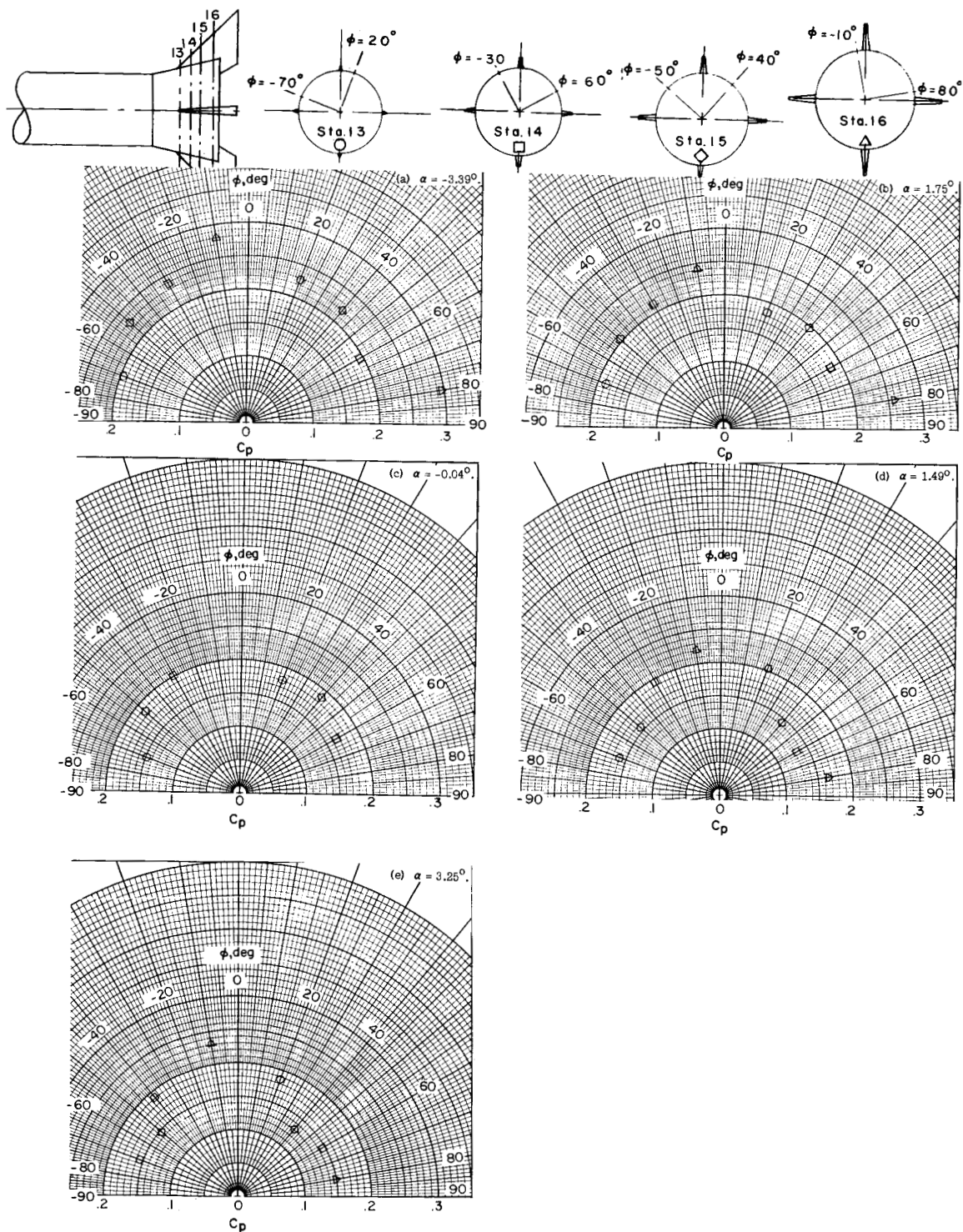


Figure 11.- Variation of C_p with ϕ for four longitudinal stations on a 13° base flare. Bent, basic fourth-stage model; Reynolds number, 2.071×10^6 based on stage 1 base diameter.

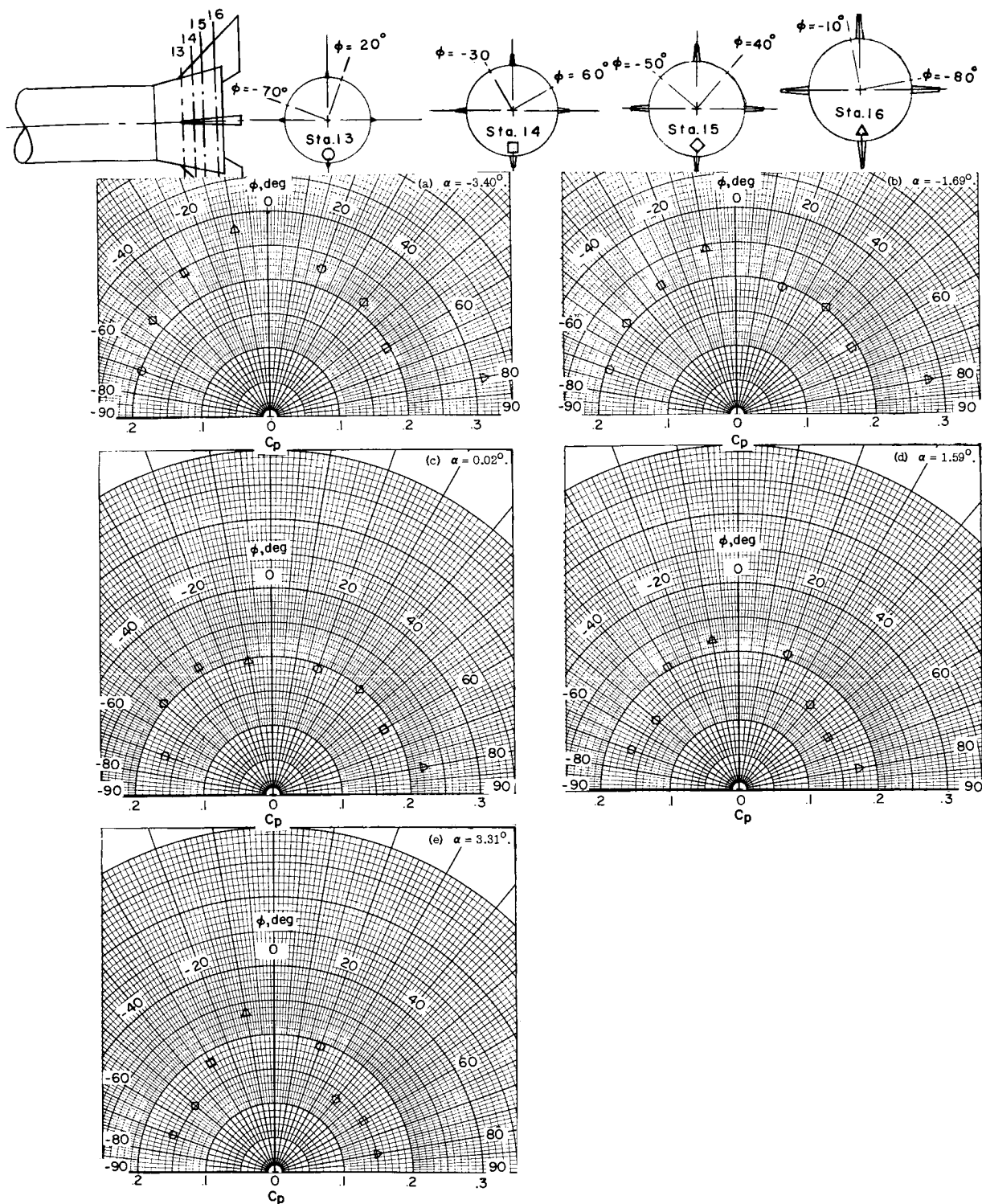


Figure 12.- Variation of C_p with ϕ for four longitudinal stations on a 13° base flare. Bent, enlarged fourth-stage model; Reynolds number, 2.071×10^6 based on stage 1 base diameter.

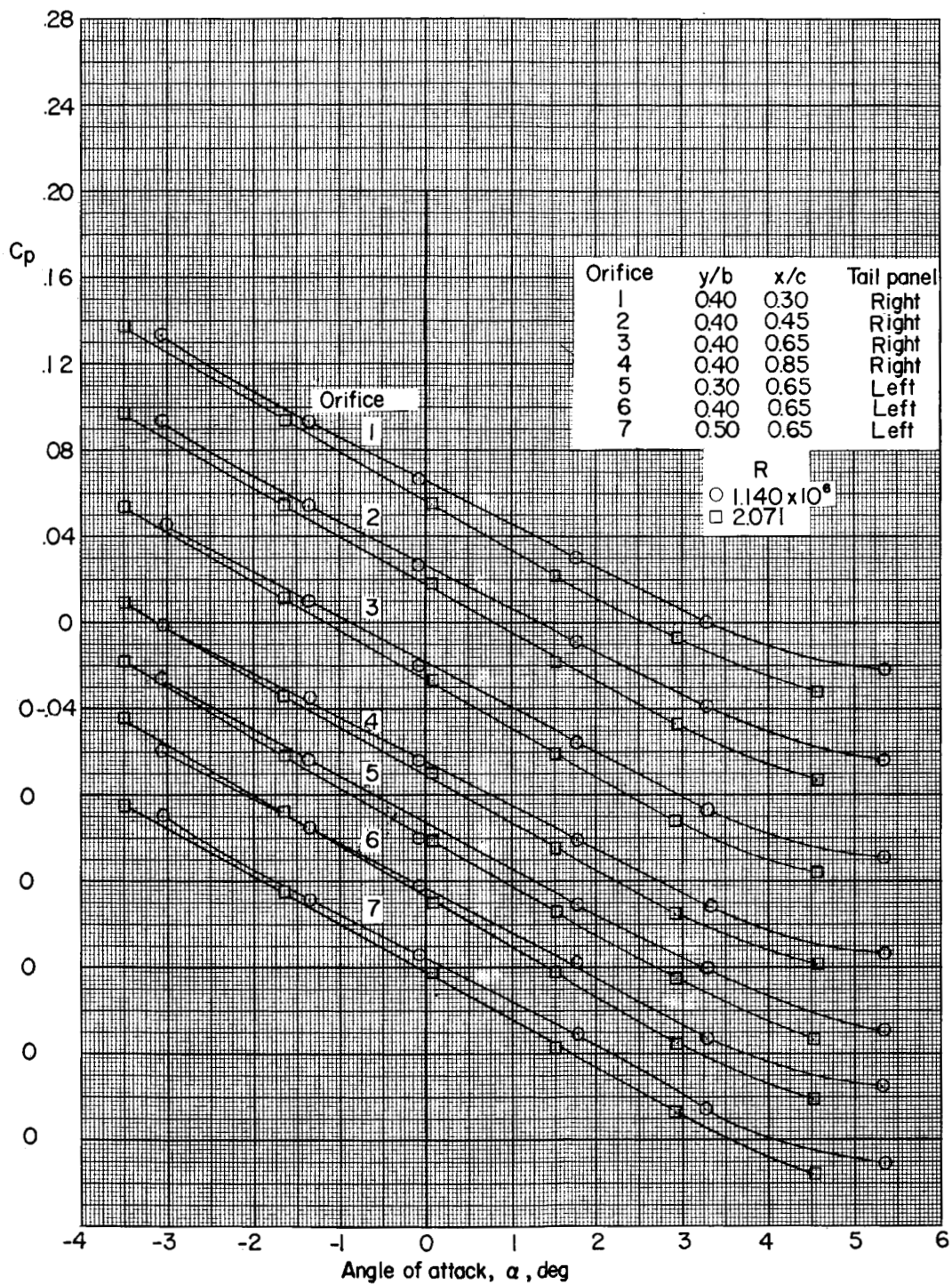


Figure 13.- Variation of C_p with angle of attack for the upper surface of the horizontal-tail panels of a straight, basic fourth-stage configuration of the Scout. 13° stage 1 base flare off; Reynolds number is based on diameter of base of stage 1.

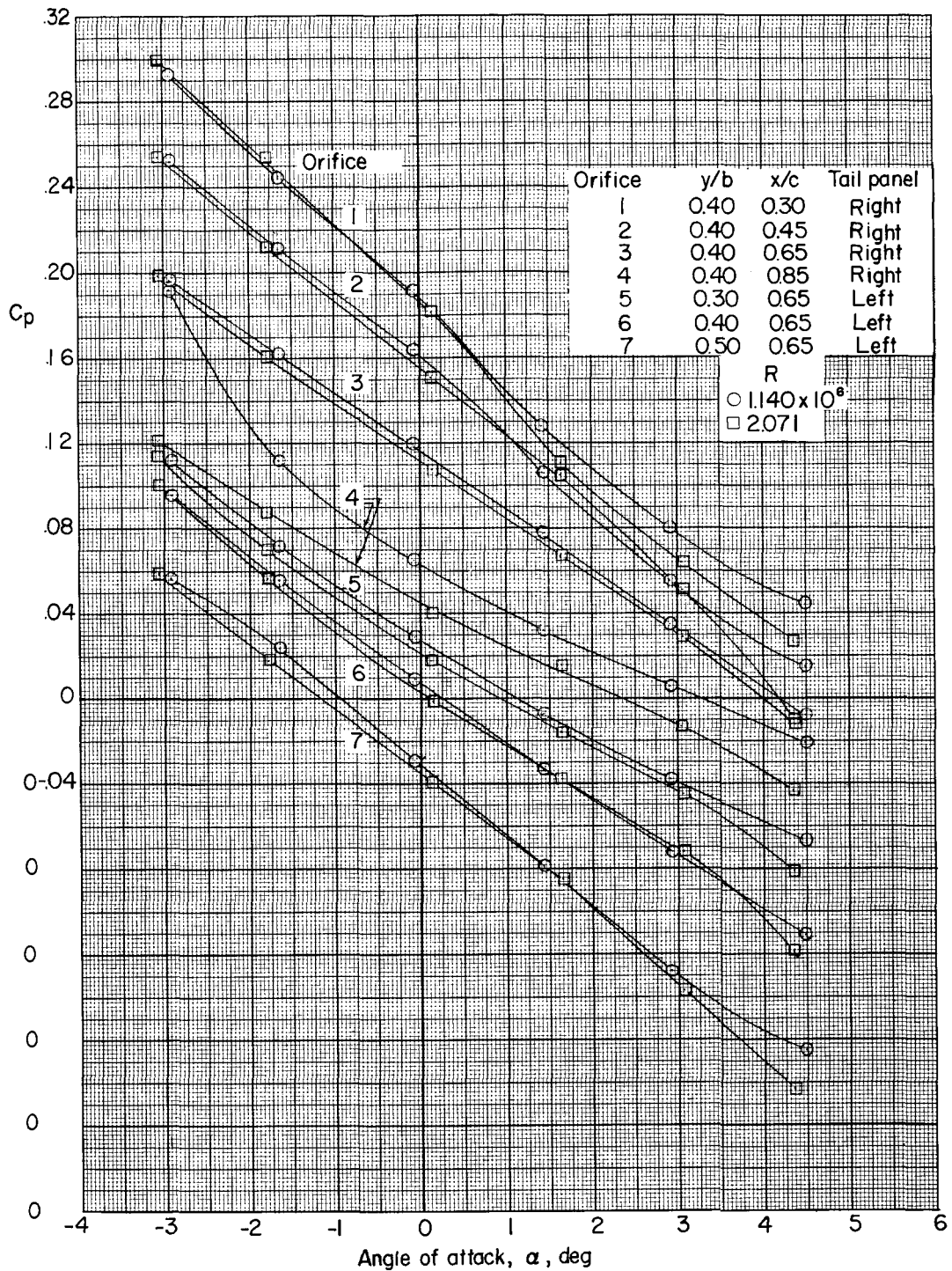
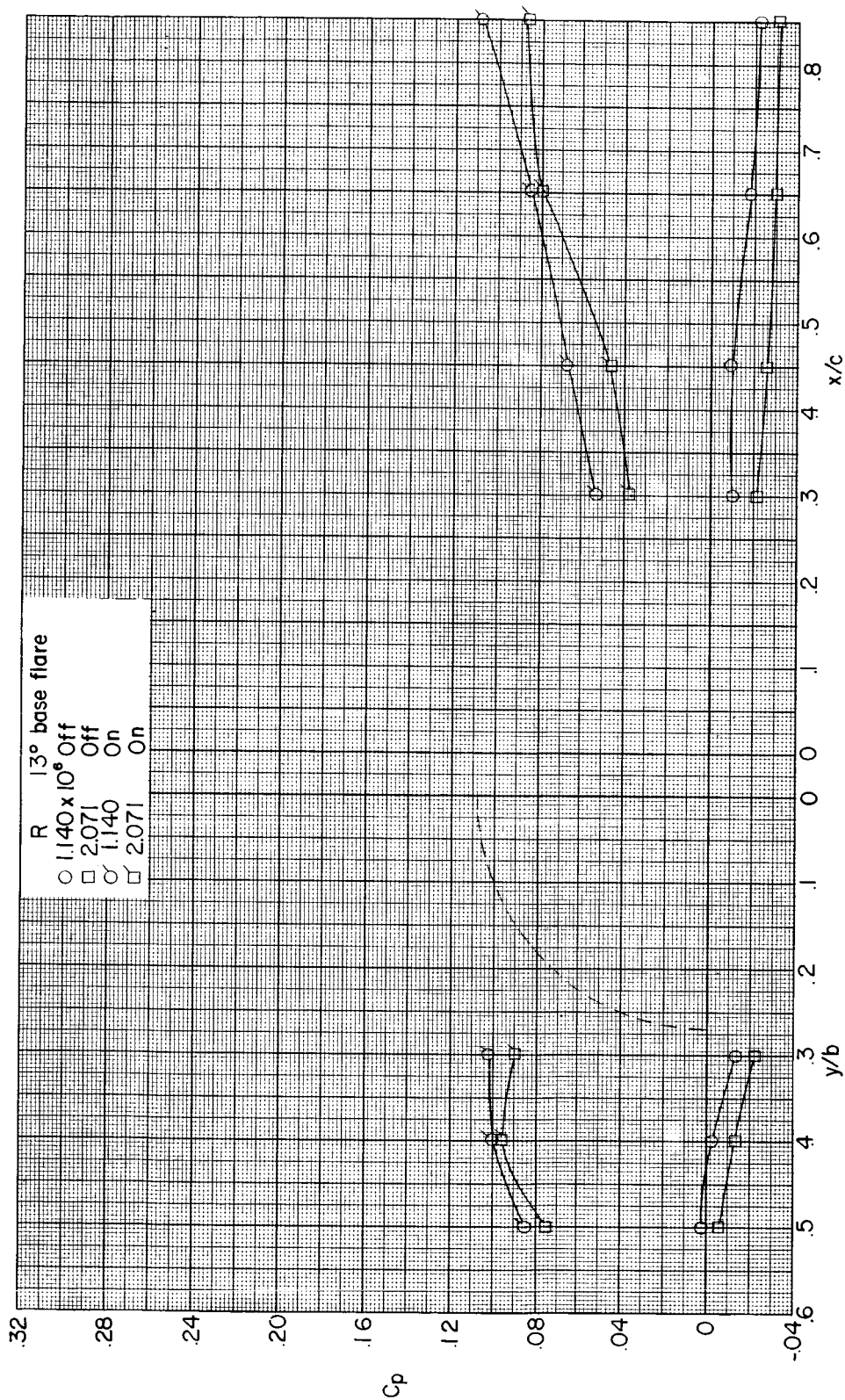


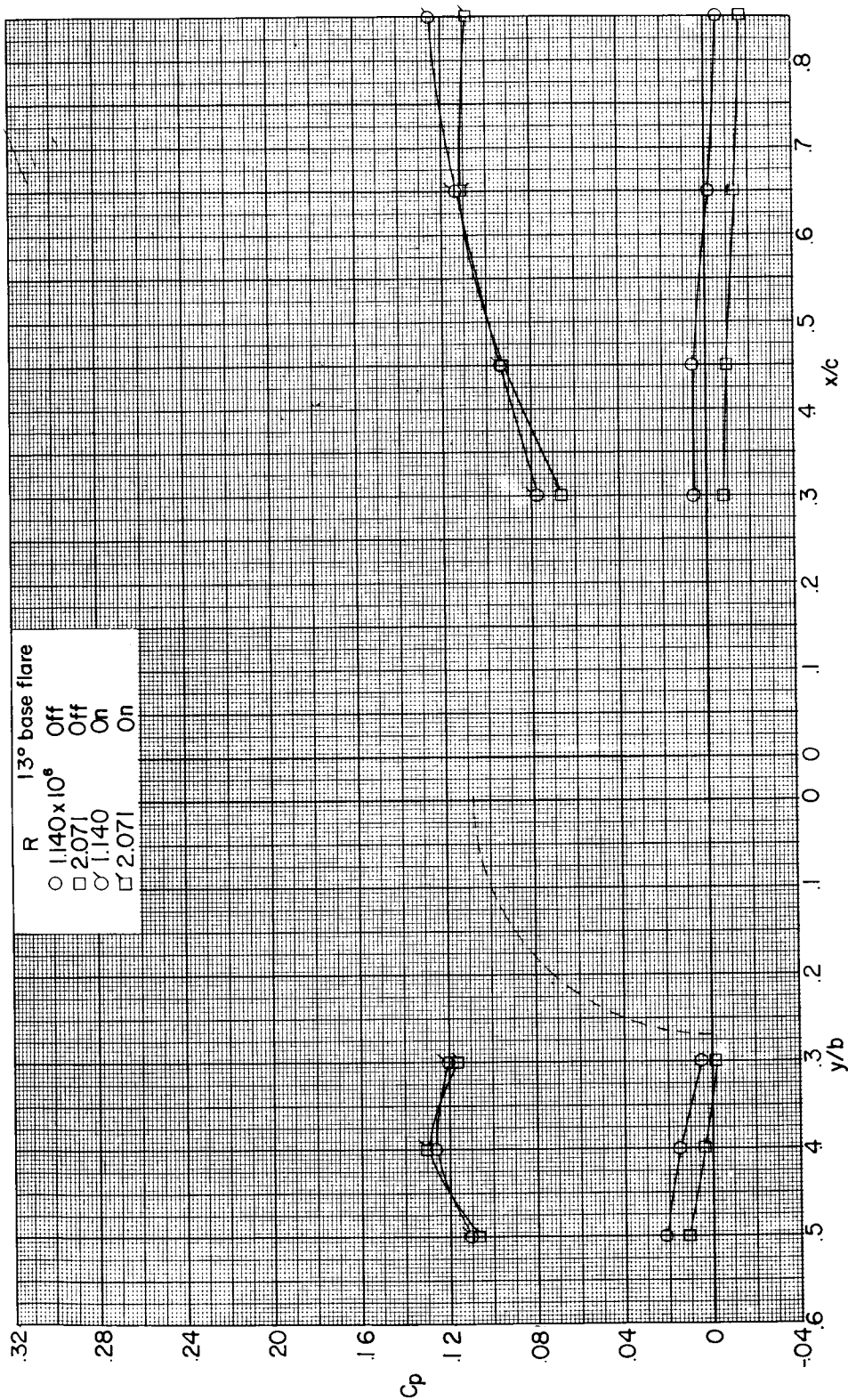
Figure 14.- Variation of C_p with angle of attack for the upper surface of the horizontal-tail panels of a straight, basic fourth-stage configuration of the Scout. 13° stage 1 base flare on; Reynolds number is based on diameter of base of stage 1.



(a) Upper surface of left panel. $x/c = 0.65$.

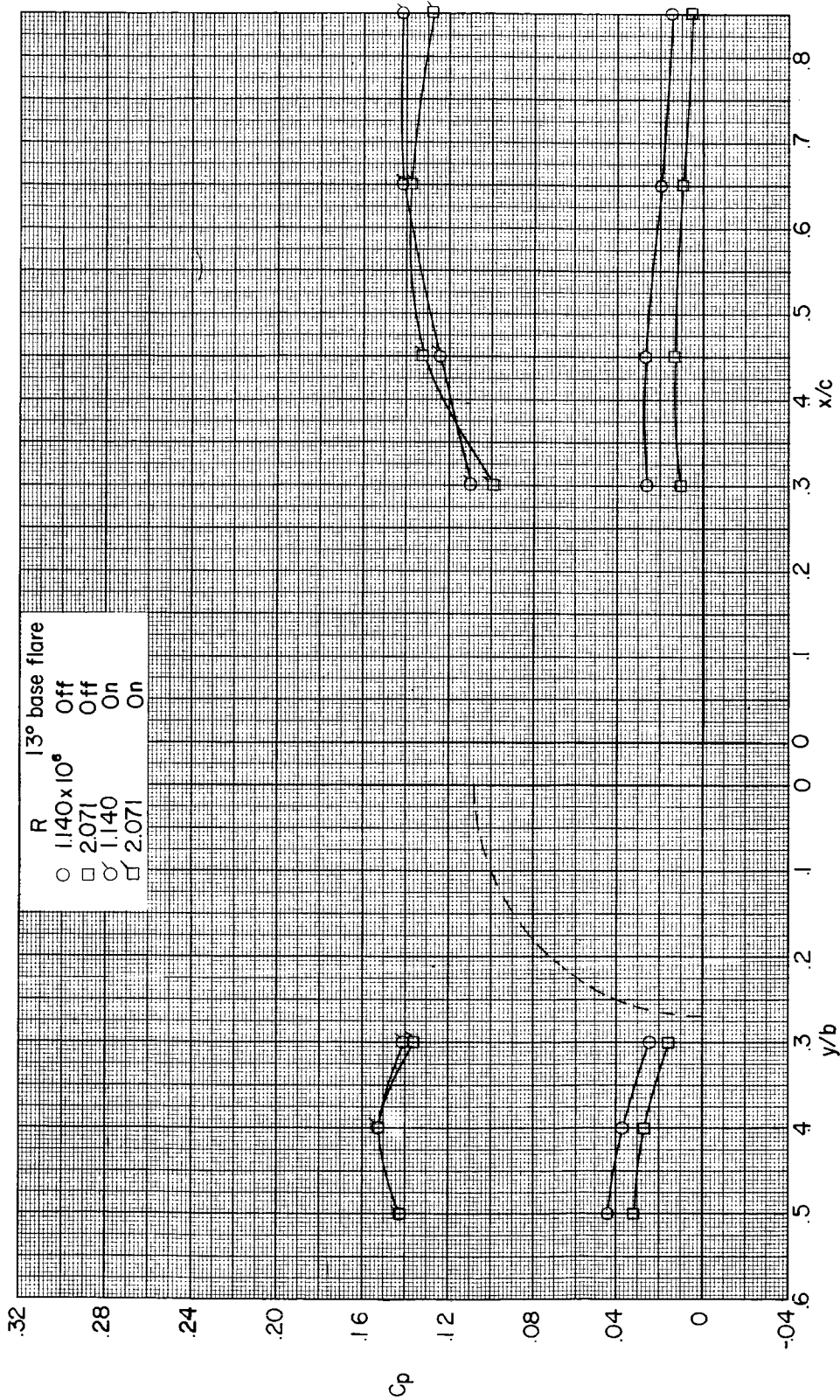
(b) Upper surface of right panel. $y/b = 0.40$.

Figure 15.- Pressure coefficients at $M = 3.10$ on the upper surface of the horizontal-tail panels of a straight, basic fourth-stage configuration of the Scout. $\alpha = 4^\circ$. (Symbols are not test points but were obtained from figures 13 and 14; dashed arc represents maximum flare diameter.)



(a) Upper surface of left panel. $x/c = 0.65$. (b) Upper surface of right panel. $y/b = 0.40$.

Figure 16.- Pressure coefficients at $M = 3.10$ on the upper surface of the horizontal-tail panels of a straight, basic fourth-stage configuration of the Scout. $\alpha = 3^\circ$. (Symbols are not test points but were obtained from figures 13 and 14; dashed arc represents maximum flare diameter.)



(a) Upper surface of left panel. $x/c = 0.65$.

(b) Upper surface of right panel. $y/b = 0.40$.

Figure 17.- Pressure coefficients at $M = 3.10$ on the upper surface of the horizontal-tail panels of a straight, basic fourth-stage configuration of the Scout. $\alpha = 2^\circ$. (Symbols are not test points but were obtained from figures 13 and 14; dashed arc represents maximum flare diameter.)

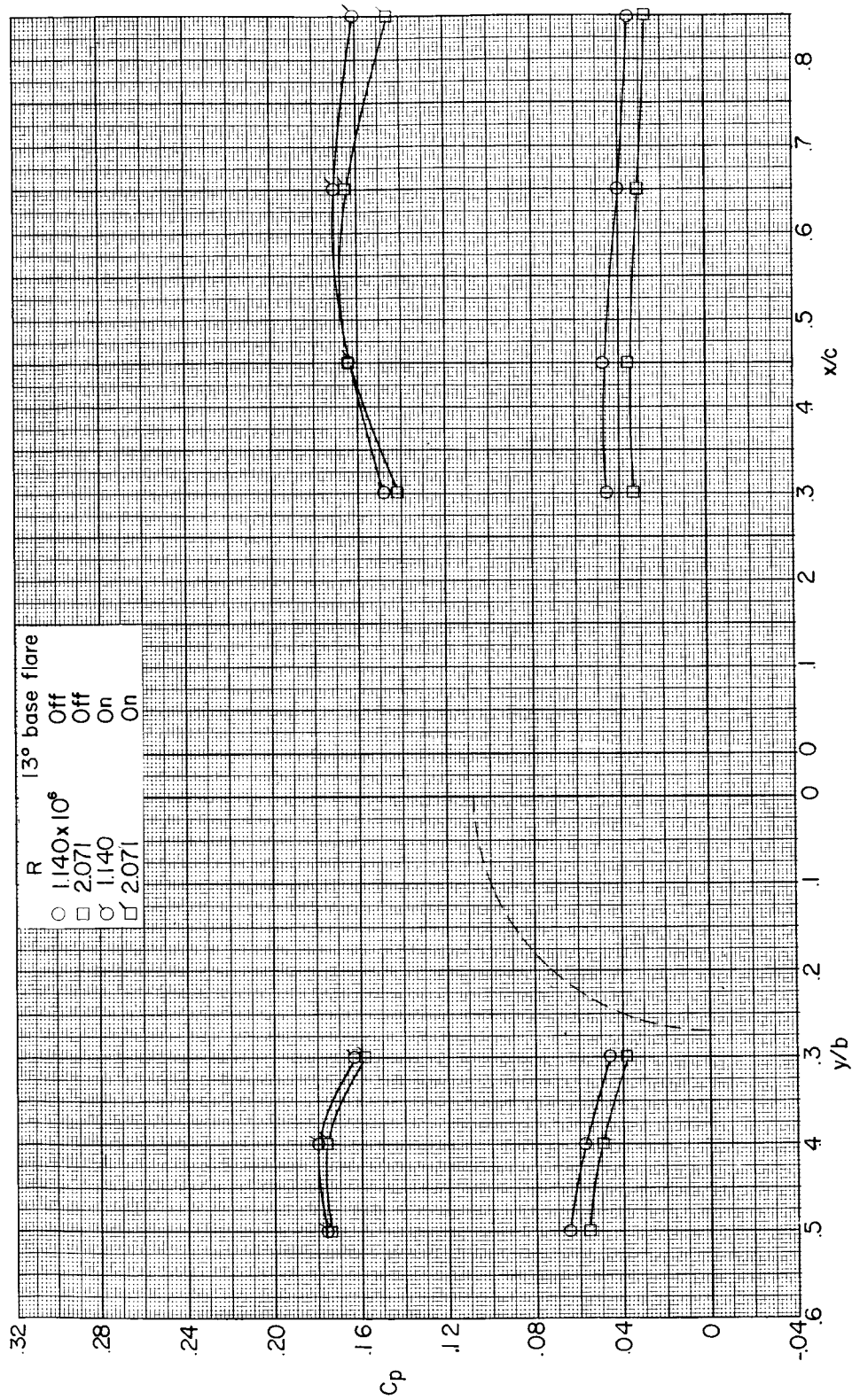
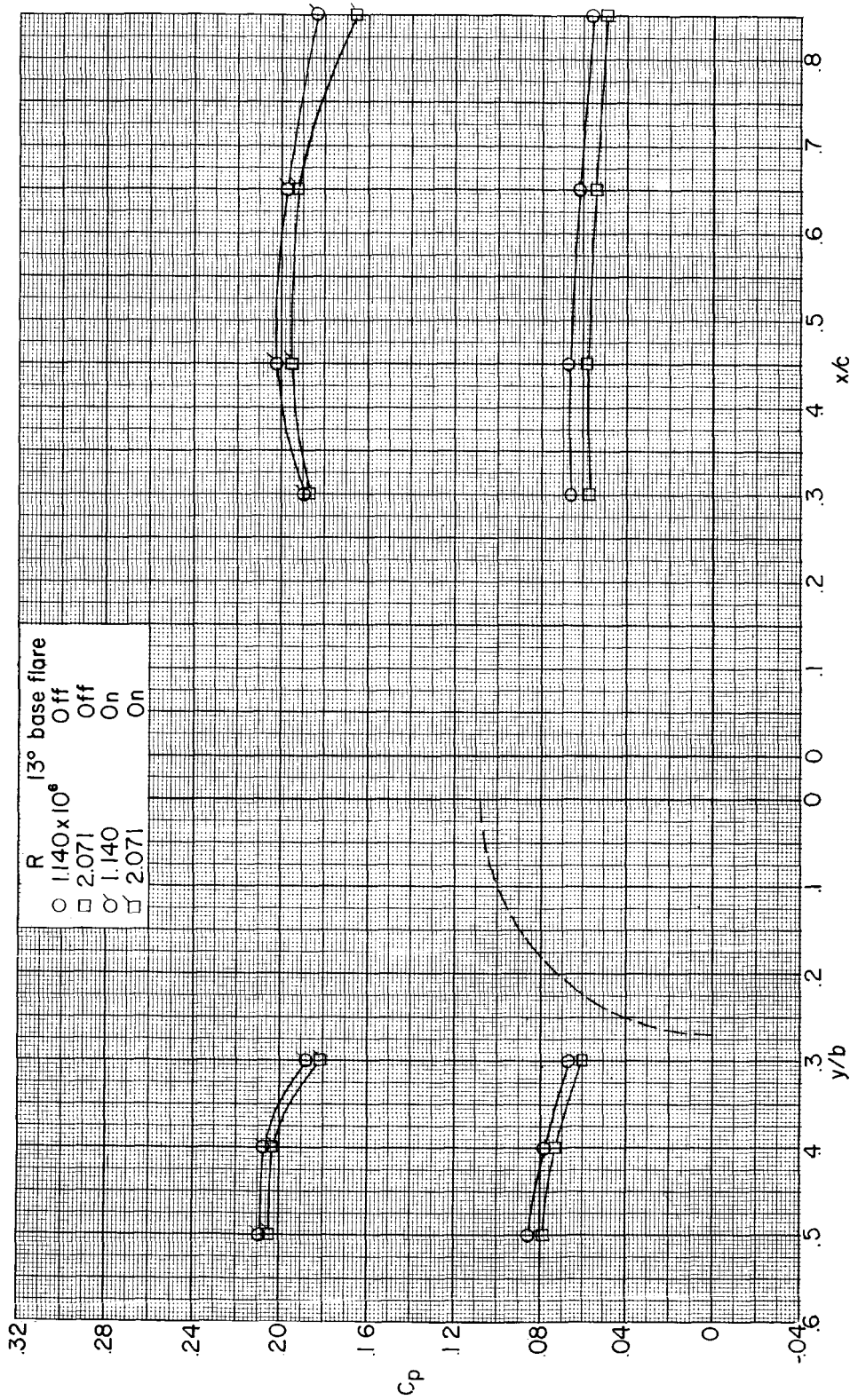
(a) Upper surface of left panel. $x/c = 0.65$.(b) Upper surface of right panel. $y/b = 0.40$.

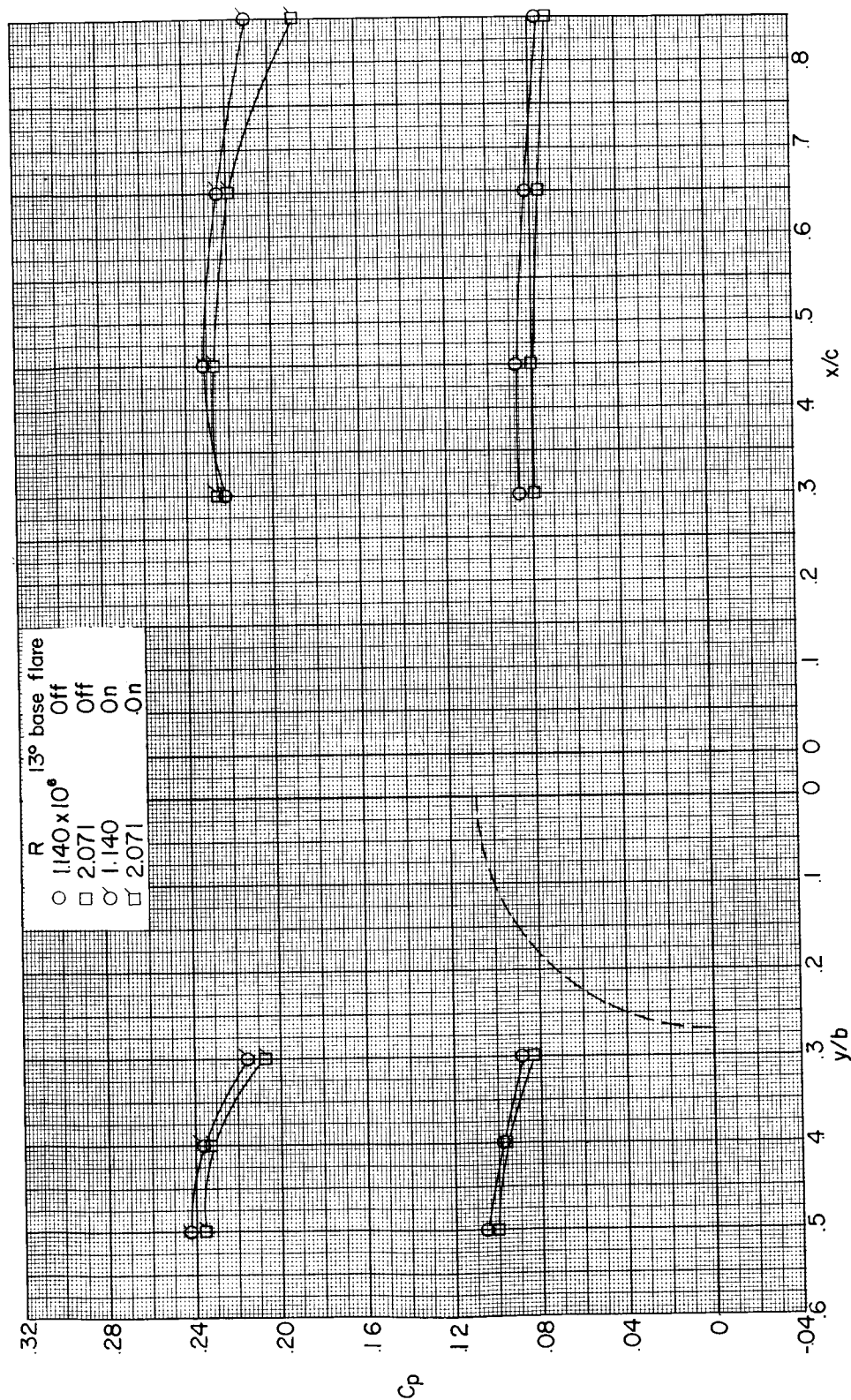
Figure 18.- Pressure coefficients at $M = 3.10$ on the upper surface of the horizontal-tail panels of a straight, basic fourth-stage configuration of the Scout. $\alpha = 10^\circ$. (Symbols are not test points but were obtained from figures 13 and 14; dashed arc represents maximum flare diameter.)



(a) Upper surface of left panel. $x/c = 0.65$.

(b) Upper surface of right panel. $y/b = 0.40$.

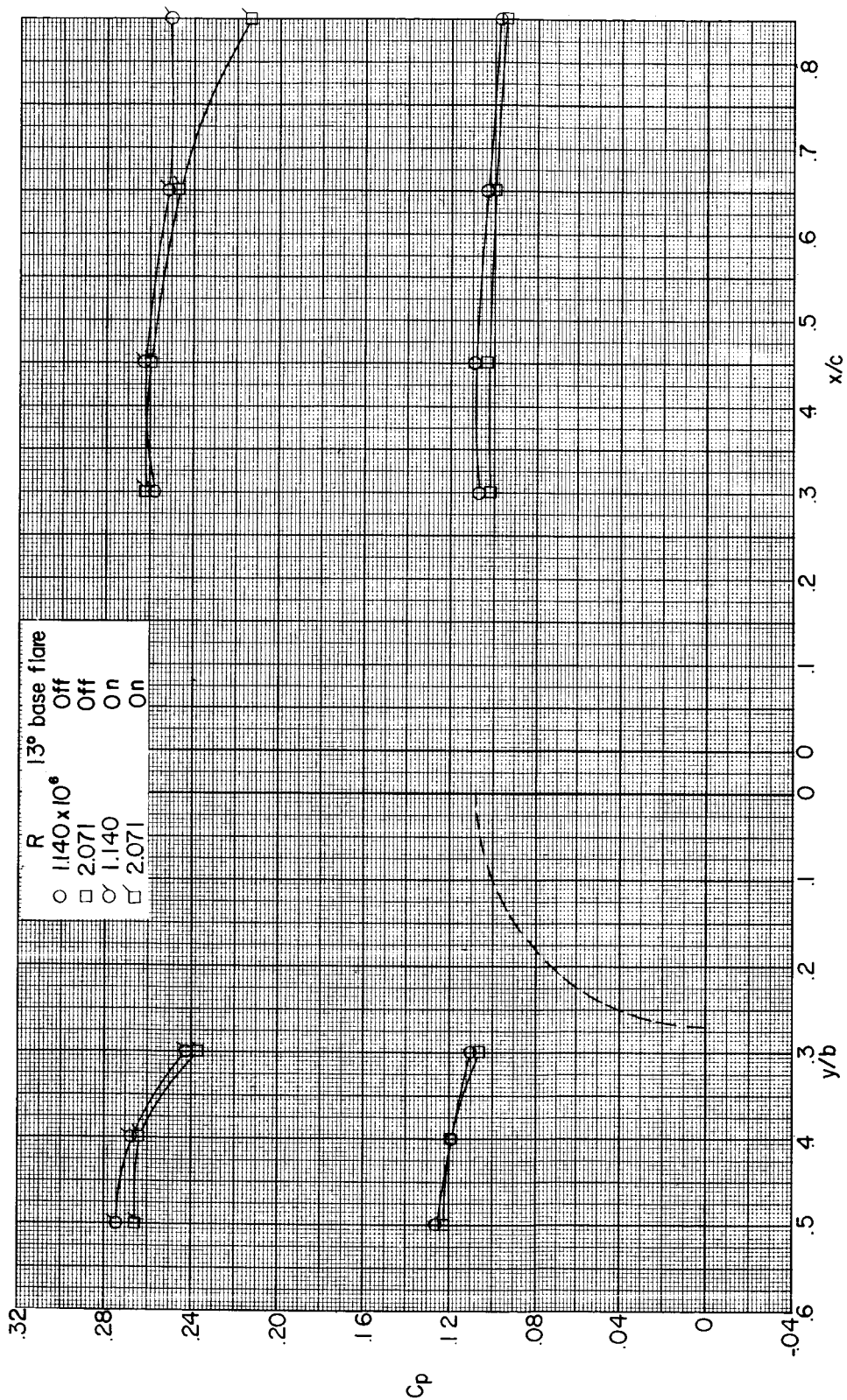
Figure 19.- Pressure coefficients at $M = 3.10$ on the upper surface of the horizontal-tail panels of a straight, basic fourth-stage configuration of the Scout. $\alpha = 0^\circ$. (Symbols are not test points but were obtained from figures 13 and 14; dashed arc represents maximum flare diameter.)



(a) Upper surface of left panel. $x/c = 0.65$.

(b) Upper surface of right panel. $y/b = 0.40$.

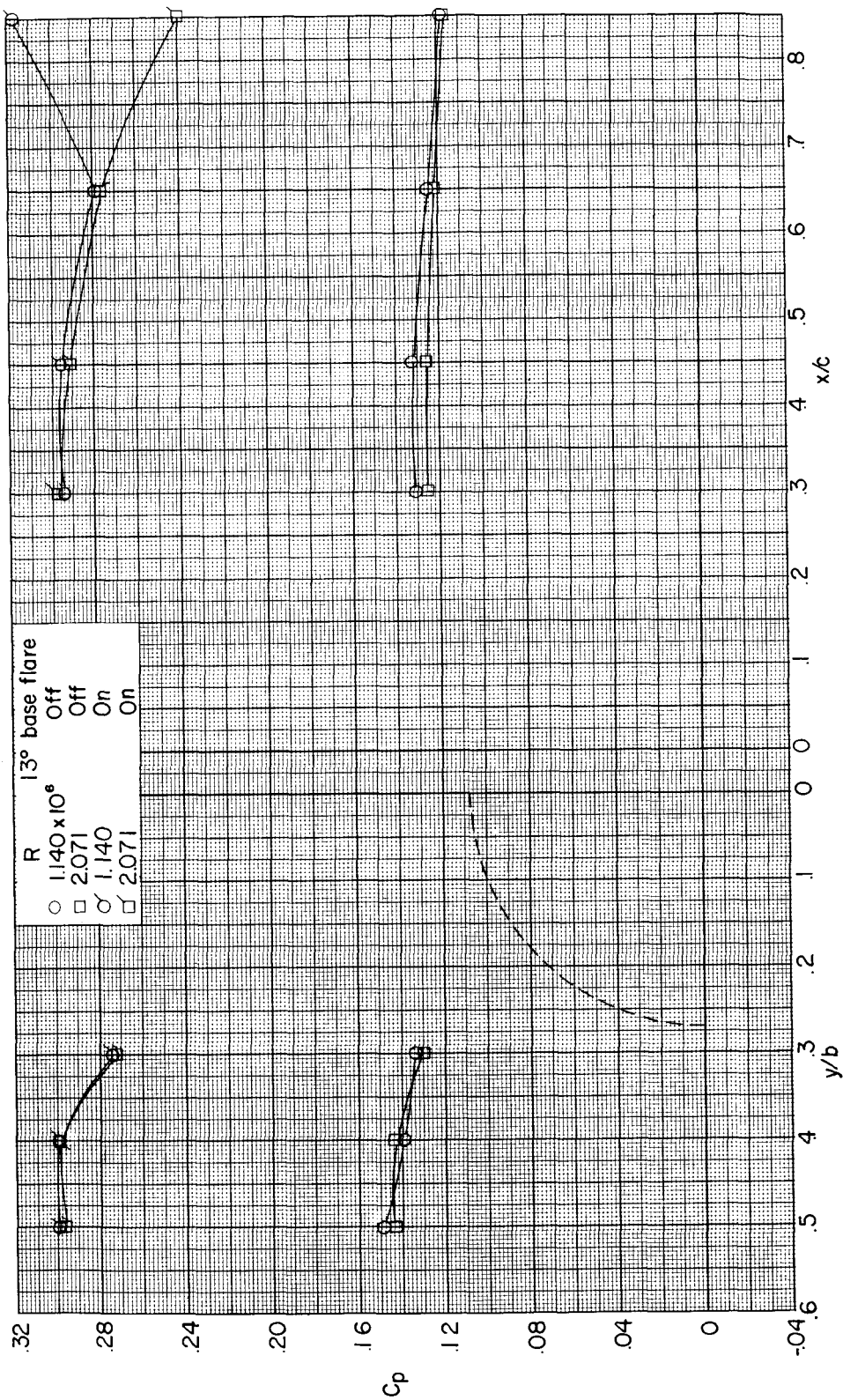
Figure 20.- Pressure coefficients at $M = 3.10$ on the upper surface of the horizontal-tail panels of a straight, basic fourth-stage configuration of the Scout. $\alpha = -10^\circ$. (Symbols are not test points but were obtained from figures 13 and 14; dashed arc represents maximum flare diameter.)



(a) Upper surface of left panel. $x/c = 0.65$.

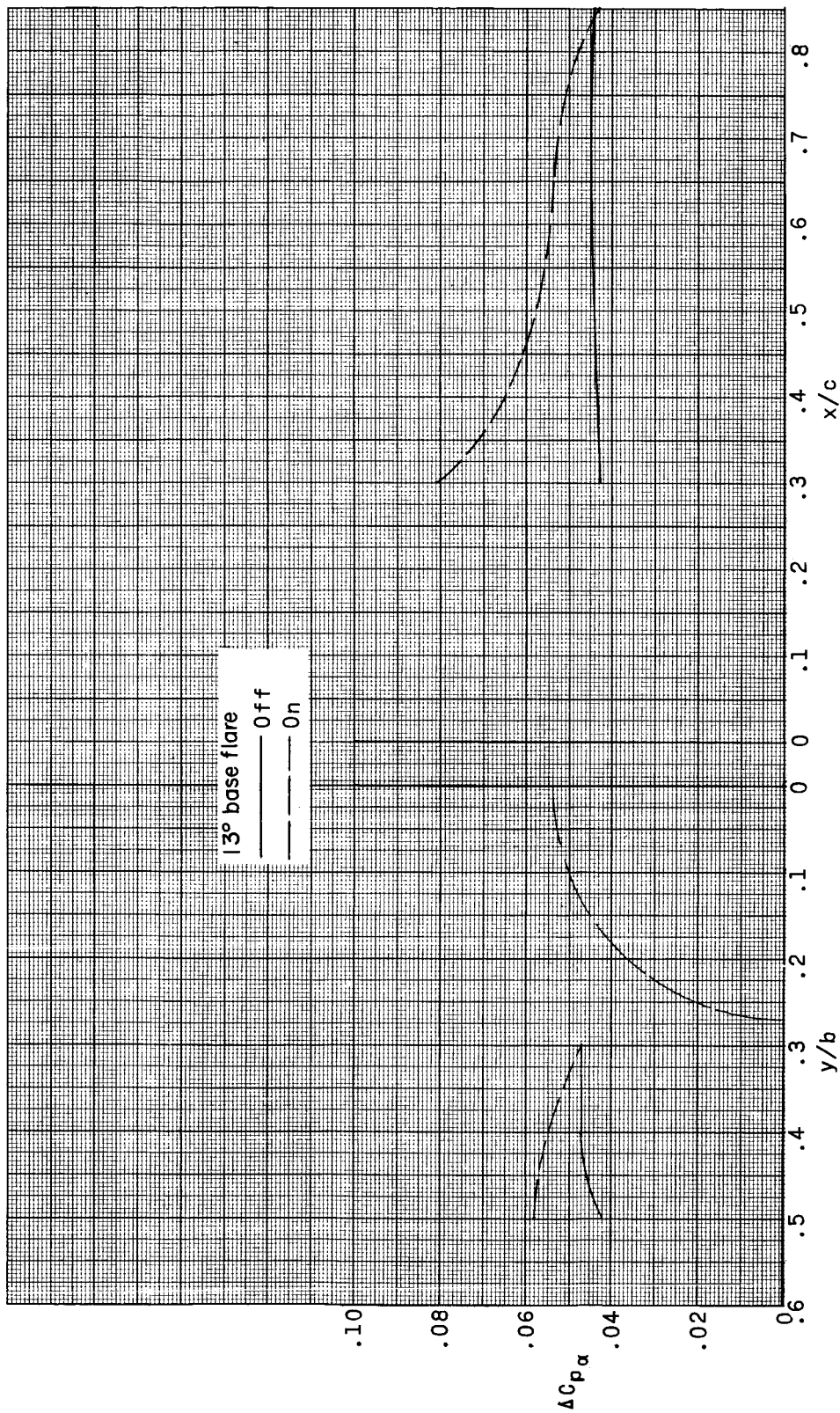
(b) Upper surface of right panel. $y/b = 0.40$.

Figure 21.- Pressure coefficients at $M = 3.10$ on the upper surface of the horizontal-tail panels of a straight, basic fourth-stage configuration of the Scout. $\alpha = -2^\circ$. (Symbols are not test points but were obtained from figures 13 and 14; dashed arc represents maximum flare diameter.)



(a) Upper surface of left panel. $x/c = 0.65$. (b) Upper surface of right panel. $y/b = 0.40$.

Figure 22.- Pressure coefficients at $M = 3.10$ on the upper surface of the horizontal-tail panels of a straight, basic fourth-stage configuration of the Scout. $\alpha = -30^\circ$. (Symbols are not test points but were obtained from figures 13 and 14; dashed arc represents maximum flare diameter.)



(a) Left panel. $x/c = 0.65$.

(b) Right panel. $y/b = 0.40$.

Figure 23.- Effect of flare on $\Delta C_{p\alpha}$ for several locations on the horizontal-tail panels of a straight, basic fourth-stage configuration of the Scout. $R = 2.071 \times 10^6$ based on stage 1 base diameter. Data obtained by assuming $C_{p,L}$ at $\alpha = C_{p,U}$ at $-\alpha$.

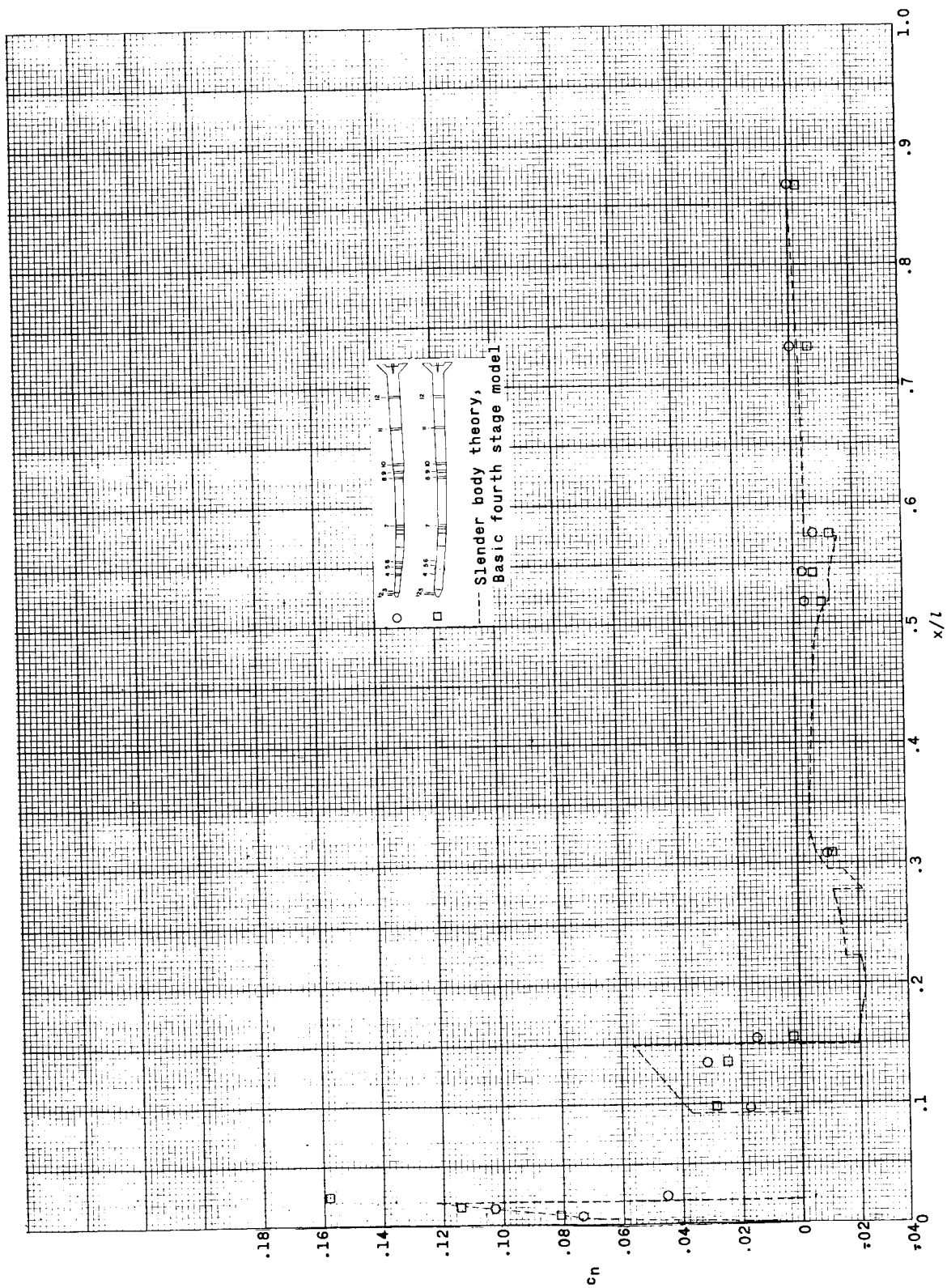


Figure 24.- Variation of c_n with x/l for bent configurations at $\alpha = 0^\circ$. Values are average of data for base flare off and on.

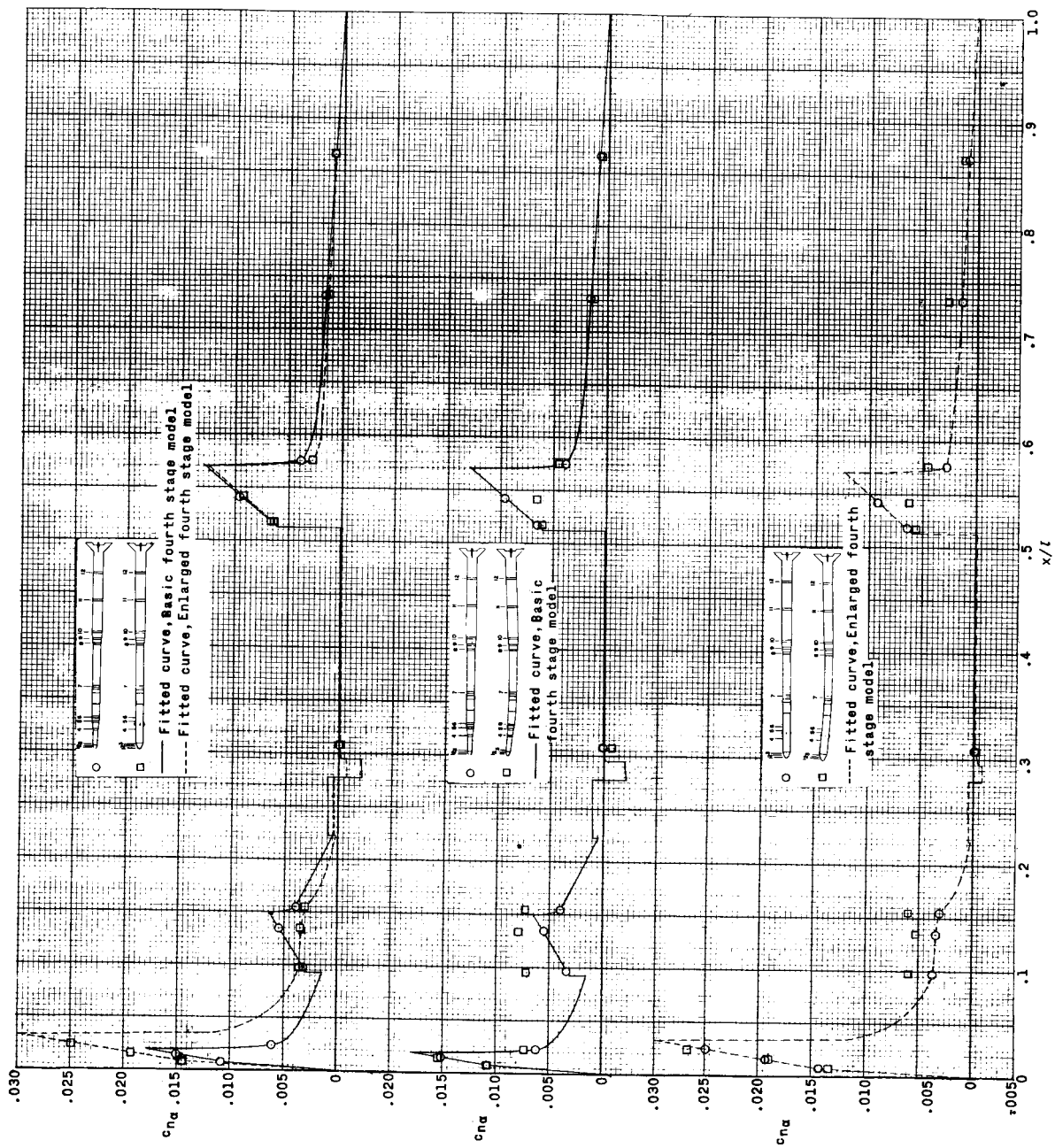


Figure 25.- Variation of $c_{n\alpha}$ with x/l for straight and bent configurations. Values are average of data for base flare off and on.

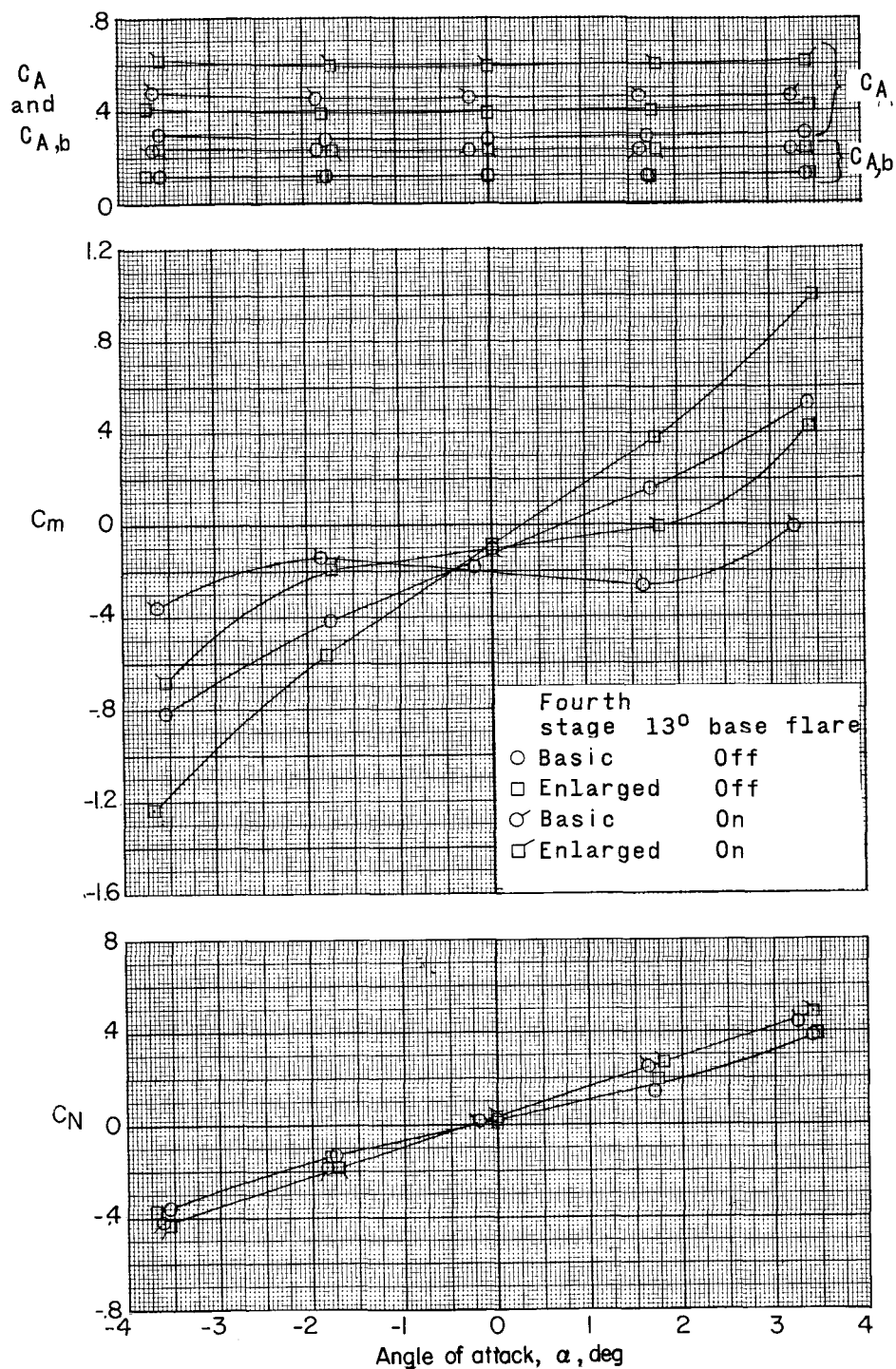


Figure 26.- Effect of fourth-stage size and a 13° base flare on the variation of aerodynamic coefficients with angle of attack of a complete straight 0.02655-scale model of the Scout. $R = 2.071 \times 10^6$ based on base diameter of stage 1.